The Astrophysical Journal, 997:261 (16pp), 2026 February 1 https://doi.org/10.3847/1538-4357/ae279b

The New Status Qvo? SN 2021qvo Is Another 2003fg-like Type Ia Supernova with a Rising Light-curve Bump

I. A. Abreu Paniagua[1,2], W. B. Hoogendam[1], D. O. Jones[3], G. Dimitriadis[4], R. J. Foley[5], C. Gall[6], J. O'Brien[7], K. Taggart[5], C. R. Angus[8], C. Ashall[1], K. Auchettl[5,9], D. A. Coulter[10,11], K. W. Davis[5], T. de Boer[1], A. Do[12], H. Gao[1], L. Izzo[6,13], C.-C. Lin[1], T. B. Lowe[1], Z. Lai[5,14], R. Kaur[5], M. Y. Kong[1], A. Rest[10,11], M. R. Siebert[11], S. K. Yadavalli[15], Y. Zenati[10,11,16,17], and Q. Wang[18,19]

[1] Institute for Astronomy, University of Hawai'i, 2680 Woodlawn Drive, Honolulu, HI 96822, USA; iabreu_paniagua@uri.edu
[2] Department of Physics, University of Rhode Island, 2 Lippitt Rd, Kingston, RI, 02881, USA
[3] Institute for Astronomy, University of Hawai'i, 640 N. Aohoku Pl., Hilo, HI 96720, USA
[4] Department of Physics, Lancaster University, Lancaster, LA1 4YB, UK
[5] Department of Astronomy and Astrophysics, University of California, Santa Cruz, CA 95064, USA
[6] DARK, Niels Bohr Institute, University of Copenhagen, Jagtvej 128, 2200 Copenhagen, Denmark
[7] Department of Astronomy, University of Illinois at Urbana-Champaign, 1002 W. Green St., IL 61801, USA
[8] Astrophysics Research Centre, School of Mathematics and Physics, Queen's University Belfast, Belfast BT7 1NN, UK
[9] School of Physics, The University of Melbourne, VIC 3010, Australia
[10] Department of Physics and Astronomy, The Johns Hopkins University, Baltimore, MD 21218, USA
[11] Space Telescope Science Institute, Baltimore, MD 21218, USA
[12] Institute of Astronomy and Kavli Institute for Cosmology, Madingley Road, Cambridge, CB3 0HA, UK
[13] INAF, Osservatorio Astronomico di Capodimonte, Salita Moiariello 16, I-80131 Napoli, Italy
[14] Las Cumbres Observatory, 6740 Cortona Drive, Suite 102, Goleta, CA 93117-5575, USA
[15] Center for Astrophysics — Harvard & Smithsonian, 60 Garden St., Cambridge, MA 02138-1516, USA
[16] Astrophysics Research Center of the Open University (ARCO), The Open University of Israel, Ra'anana 4353701, Israel
[17] Department of Natural Sciences, The Open University of Israel, Ra'anana 4353701, Israel
[18] Department of Physics and Kavli Institute for Astrophysics and Space Research, Massachusetts Institute of Technology, 77 Massachusetts Avenue, Cambridge, MA 02139, USA
[19] TESS-ULTRASAT Joint Postdoctoral Fellow

Received 2025 August 25; revised 2025 November 12; accepted 2025 November 25; published 2026 January 28

Abstract

In recent years, multiple Type Ia supernovae (SNe Ia) have been observed with "bumps" in their rising light curves shortly after the explosion. Here, we present SN 2021qvo: an SN Ia that exhibits a clear early bump in photometry obtained by the Young Supernova Experiment. Photometric and spectroscopic observations of SN 2021qvo show that it has a broader light curve, higher peak luminosity, shallower Si II λ5972 pseudoequivalent width, and lower ejecta velocities than normal SNe Ia, which are all consistent with the characteristics of the 2003fg-like (often called "super-Chandrasekhar") SN subtype. Including SN 2021qvo, just four known 2003fg-like SNe Ia have sufficient prepeak data to reveal a rising light-curve bump, and all four have bump detections. A host-galaxy analysis reveals that SN 2021qvo exploded in a low-mass galaxy $\log(M_*/M_\odot) = 7.83^{+0.17}_{-0.24}$, also consistent with other members of this class. The current leading early bump 2003fg-like SN Ia progenitor model involves an interaction between the circumstellar material (CSM) and the SN ejecta. We test the validity of this theory by modeling the early bump and subsequent light-curve evolution of SN 2021qvo with the Modular Open Source Fitter for Transients. We find that the bump can be modeled with a best-fit CSM mass in the range $M_{\rm CSM} = 3.31-8.51 \times 10^{-3} M_\odot$. SN 2021qvo adds to the small but growing number of 2003fg-like SNe Ia with rising light-curve bumps; as the number of these SNe Ia with CSM estimates continues to grow, population-level inferences about the CSM distribution will be able to constrain the progenitor scenario for these SNe Ia.

Unified Astronomy Thesaurus concepts: Type Ia supernovae (1728)

Materials only available in the online version of record: data behind figure, machine-readable tables

1. Introduction

Type Ia supernovae (SNe Ia) follow a strongly correlated luminosity-width relation (LWR) that relates the light-curve shape of an SN Ia to its intrinsic luminosity, allowing for distances to be calculated with high precision (M. M. Phillips 1993). SNe Ia can be used to measure cosmological parameters with high precision using distances derived from this relationship, including the Hubble constant (e.g., C. R. Burns et al. 2018; W. L. Freedman et al. 2019; A. G. Riess et al. 2022; W. Freedman et al. 2024) and the dark energy equation of state parameter (e.g., M. Betoule et al. 2014; D. M. Scolnic et al. 2018; D. O. Jones et al. 2019; D. Brout et al. 2022; DES Collaboration et al. 2024).

While there is broad consensus that SNe Ia result from an exploding carbon–oxygen (CO) white dwarf (WD) star (F. Hoyle & W. A. Fowler 1960), there is a large diversity of proposed models explaining SNe Ia, each with their own unique progenitor scenario and explosion mechanism (see A. J. Ruiter & I. R. Seitenzahl 2025 for a recent review). SNe Ia progenitor channels include the single degenerate scenario containing a CO WD and a nondegenerate companion

(e.g., J. Whelan & I. Iben 1973; K. Nomoto 1982a), the double degenerate scenario containing two degenerate CO WDs, a CO WD and a He WD, or a CO WD and a HeCO WD (e.g., K. Nomoto 1980; I. J. Iben & A. V. Tutukov 1984; H. B. Perets et al. 2019), and the core degenerate scenario containing a CO WD and an asymptotic giant branch star (e.g., A. Kashi & N. Soker 2011).

Each progenitor scenario has several possible explosion mechanisms that could result in an SN Ia. In the single degenerate scenario, the CO WD accretes material from the nondegenerate companion star (either a red giant star or a main-sequence star) until a thermonuclear runaway explosion occurs (generally when the CO WD nears the Chandrasekhar mass; J. Whelan & I. Iben 1973; K. Nomoto et al. 1984). Accretion-triggered explosions can also occur in the double degenerate scenario (e.g., K. Nomoto 1982a); a detonation of accreting or built-up surface helium may send a converging shock into the CO WD, causing central carbon ignition (and thus an SN Ia, e.g., K. Nomoto 1980, 1982b; E. Livne 1990; K. J. Shen & K. Moore 2014). Finally, dynamical or violent mergers may also cause an SN Ia in the double degenerate scenario (e.g., I. J. Iben & A. V. Tutukov 1984; R. F. Webbink 1984; C. Raskin et al. 2009; S. Rosswog et al. 2009; ; R. Pakmor et al. 2010; L. A. Kwok et al. 2023, 2024; M. R. Siebert et al. 2024).

Most SNe Ia are spectroscopically and photometrically "normal" (e.g., D. D. Desai et al. 2024) with similar photometric and spectroscopic features (e.g., N. Morrell et al. 2024; although at the earliest stages show significant diversity, W. B. Hoogendam et al. 2025a). However, a growing number of SNe Ia have been discovered with different observational properties, which may arise from differences in the underlying progenitor scenario and/or explosion mechanism. While some SN Ia subtypes follow an LWR (i.e., 1991bg-like and 1991T-like SNe Ia, A. V. Filippenko et al. 1992; M. M. Phillips et al. 1992; B. Leibundgut et al. 1993), other subtypes do not. These include 2002cx-like (W. Li et al. 2003), 2002es-like (M. Ganeshalingam et al. 2012), and 2003fg like SNe Ia (D. A. Howell et al. 2006). Because of deviations in parameters like peak absolute magnitude (abs mag) and light-curve decline rate, such SNe Ia are not always standardizable for SN cosmology. Still, these peculiar objects offer an opportunity to understand the extreme ends of the SNe Ia population.

These peculiar SN Ia subtypes are identified through a mix of photometric and spectroscopic characteristics. Several 2003fg-like SNe Ia have abnormally luminous absolute magnitudes between −19.5 and −20.4 (M. Hicken et al. 2007; R. A. Scalzo et al. 2010; G. Dimitriadis et al. 2022) and decline rate Δm_{15} values in the range of 0.7–0.9 mag (S. Taubenberger 2017; C. Ashall et al. 2021); however, we now know there is a broad diversity in this subclass with some showing more typical luminosities and decline rates (∼0–1 mag brighter E. Y. Hsiao et al. 2020; J. Lu et al. 2021). In general, 2003fg-like events are ∼1–2 mag brighter than normal SNe Ia (D. D. Desai et al. 2024) and have light-curve shapes consistent with or broader than the slowest-declining normal SNe Ia. With these properties in mind, common photometric diagnostic features are a primary *i*-band maximum after the primary *B*-band maximum, weak or missing *i*-band secondary maximum, and a broad light curve (C. Ashall et al. 2021, although the latter two are seen in only some 2003fg-like SNe Ia).

Spectroscopically, 2003fg-like SNe Ia also exhibit different features than normal SNe Ia. The early time spectra of 2003fg-like SNe Ia have weaker Ca II features and prominent O I and C II features (S. Taubenberger 2017; C. Ashall et al. 2021) and have higher UV flux than normal SNe Ia (W. B. Hoogendam et al. 2024; S. Bhattacharjee et al. 2025). In general, the C II $\lambda\lambda$6580,7234 features are especially strong for up to ∼2 weeks after maximum light. At later times, 2–4 weeks after maximum light, 2003fg-like SN Ia spectra are dominated by Fe II slightly earlier than for normal SNe Ia (J. M. Silverman et al. 2011; S. Taubenberger et al. 2011; N. K. Chakradhari et al. 2014; J. T. Parrent et al. 2016). Other spectroscopic diagnostics to identify an SNe as 2003fg-like include a lack of an *H*-band break at +10 days in the near-infrared (NIR) spectra and a low ionization state in nebular-phase spectra. Features common, but not ubiquitous in the 2003fg-like population include strong C II features after maximum light, low ejecta velocity gradients before maximum light, a lack of Ti II lines in the peak time spectra, and asymmetric NIR nebular lines (e.g., SN 2022pul; L. A. Kwok et al. 2024; M. R. Siebert et al. 2024; J. O'Hora et al. 2025).

Recently, three 2003fg-like SNe Ia with sufficiently early detections have been discovered with bump-like features in their early time emission[20]: SNe 2020hvf (J.-a. Jiang et al. 2021), 2021zny (G. Dimitriadis et al. 2023), and 2022ilv (S. Srivastav et al. 2023). These three SNe Ia are the only three known 2003fg-like SNe Ia with sufficient observations to ascertain the presence of a rising light-curve bump, suggesting these bump features may be common or even ubiquitous in 2003fg-like SNe Ia. Furthermore, these bumps have solely been observed in 2003fg-like SNe Ia and in another SN Ia subtype, 2002es-like SNe Ia, potentially suggesting these objects are linked (W. B. Hoogendam et al. 2024).

Many models attempt to explain the origin of rising light-curve bumps in SNe Ia. While the interaction between SN ejecta and a nondegenerate companion in the single degenerate scenario (e.g, D. Kasen 2010; K. Maeda et al. 2014; M. Kutsuna & T. Shigeyama 2015) has been ruled out for these objects (G. Dimitriadis et al. 2023; S. Srivastav et al. 2023; W. B. Hoogendam et al. 2024), varying radial distributions of ^{56}Ni (e.g., A. L. Piro & V. S. Morozova 2016; M. R. Magee & K. Maguire 2020), the interaction between SN ejecta and circumstellar material (CSM; e.g., N. Levanon et al. 2015; A. L. Piro & V. S. Morozova 2016; N. Levanon & N. Soker 2017; K. Maeda et al. 2018), or a surface He detonation (e.g., J.-a. Jiang et al. 2017; K. Maeda et al. 2018; A. Polin et al. 2019; S.-C. Leung & K. Nomoto 2020; S.-C. Leung et al. 2021) may produce an observable "bump" signature. The early colors may be too blue for significant surface ^{56}Ni from either mixing or a surface He-detonation, leaving CSM interaction as the preferred explanation (W. B. Hoogendam et al. 2024). This is consistent with the spectral and light-curve evolution, which also suggests a CSM-interacting explosion (C. Ashall et al. 2021).

In this work, we examine the photometric and spectroscopic properties of SN 2021qvo, a 2003fg-like SN Ia that adds to the class of such objects that exhibit early light-curve bumps. Section 2 presents our observations. Sections 4 and 5 contain our photometric and spectroscopic observations, respectively. In Section 6, we constrain the CSM mass and compare it to

[20] Following W. B. Hoogendam et al. (2024), we use the term "bump" to indicate a nonmonotonic rise in the SN light curve.

similar events in the literature. Finally, Section 7 summarizes the main results. Throughout, we use a flat ΛCDM cosmology with $\Omega_m = 0.3$ and $H_0 = 70\,\mathrm{km\,s^{-1}\,Mpc^{-1}}$.

2. Data

SN 2021qvo was discovered in a small, faint galaxy (see Section 3) by the Asteroid Terrestrial-impact Last Alert System (ATLAS; J. L. Tonry et al. 2018) on 2021 June 21, with an *o*-band magnitude of ∼19.5 mag (J. Tonry et al. 2021). The location of SN 2021qvo is (α, δ) = ($22^h08^m12\overset{s}{.}08$, $+07\circ07'00\overset{''}{.}78$).

The Young Supernova Experiment (YSE; D. O. Jones et al. 2021) classified SN 2021qvo 2 days after its discovery on 2021 June 23, (C. R. Angus & C. Rojas-Bravo 2021) with a classification spectrum from the Alhambra Faint Object Spectrograph and Camera on the Nordic Optical Telescope. They used `SuperFit` (D. A. Howell et al. 2005) and SNID (S. Blondin & J. L. Tonry 2007) to classify the event as an SN Ia, finding that the transient matched the template of an SN Ia around −10 days.

2.1. Photometric Data

Photometric observations of SN 2021qvo primarily include the ATLAS "cyan" and "orange" filters (approximately equivalent to $g+r$ and $r+i$ bandpasses, respectively) and the Pan-STARRS *griz* filters, spanning from MJD ∼59346 to ∼59880. We obtained the ATLAS photometry from the online ATLAS forced photometry service (K. W. Smith et al. 2020; L. Shingles et al. 2021).[21] The ATLAS forced photometry has a detection of SN 2021qvo before discovery on June 17 at 4.7σ significance.

Before the ATLAS discovery, serendipitous prediscovery observations were taken by YSE with the Pan-STARRS Gigapixel Camera 1 (N. Kaiser & Pan-STARRS Team 2002; E. A. Pier & K. Chambers 2007). YSE is a time-domain survey using the Pan-STARRS telescopes designed to obtain *griz* light curves of transients up to $z = 0.2$. YSE can detect events as faint as ∼20.5 mag in *z* and ∼21.5 mag in *gri*, observing 1500 $\mathrm{deg^2}$ every 3 days (D. O. Jones et al. 2021). The Pan-STARRS photometry used in this manuscript has already been published in YSE DR1 (P. D. Aleo et al. 2023). As described in that data release, the Pan-STARRS photometric data collected by YSE is processed by the University of Hawai'i Institute for Astronomy's Image Processing Pipeline (E. A. Magnier et al. 2020a, 2020b). The first detection by YSE was on 2021 June 17 in the *g* and *i* bands, approximately 17 days before maximum light and ∼4 days before the ATLAS discovery. After discovery, we used the YSE-PZ interface (D. A. Coulter et al. 2023) to triage the data and organize follow-up observations of this event. See Tables 1 and 2 for the ATLAS and Pan-STARRS photometric data, respectively.

Beginning near maximum light, imaging of SN 2021qvo was also obtained in the *BVri* bands with the 1 m Nickel telescope at Lick Observatory. The images were calibrated using bias and sky flat-field frames following standard procedures. Point-spread function (PSF) photometry was performed, and photometry was calibrated using Pan-STARRS photometric standards (H. A. Flewelling et al. 2020).

[21] https://fallingstar-data.com/forcedphot/

Table 1
Photometric Measurements of SN 2021qvo from ATLAS

MJD	Filter	Magnitude	Mag err
58402.41	c	21.24	0.60
58406.37	o	21.01	0.53
58410.36	o	18.09	1.09
⋮	⋮	⋮	⋮
59592.21	o	19.86	0.59

(This table is available in its entirety in machine-readable form in the online article.)

Table 2
Photometric Measurements of SN 2021qvo from YSE

MJD	Filter	Magnitude	σ_m
59382.57	*g*	20.04	0.07
59382.57	*i*	20.25	0.08
59383.57	*g*	20.50	0.08
⋮	⋮	⋮	⋮
59527.21	*i*	21.24	0.23

(This table is available in its entirety in machine-readable form in the online article.)

2.2. Hubble Space Telescope Data

The location of SN 2021qvo was also imaged by the Hubble Space Telescope (HST; GO 16691) on MJD 59841, approximately 440 days after *g*-band maximum, in the F555W and F850LP filters. To see if these data could place meaningful constraints on the presence of CSM interacting with the SN ejecta at late times (i.e., M. L. Graham et al. 2019), we aligned the HST imaging to Pan-STARRS *r* using 13 stars visible in all images. Our astrometric alignment procedures followed those of C. R. Angus et al. (2024), including star detection via SExtractor (E. Bertin & S. Arnouts 1996) to identify common stars in all images. Specifically, we removed sources within 20 pixels of the edges of the images, required sources to have ellipticity <0.5 and FWHM less than 5 times the mode of the FWHM distribution of detected sources, in order to exclude extended or irregular objects. After applying these criteria, we visually confirmed 13 high-confidence point sources common to both the HST and Pan-STARRS images and used these for the transformation. We performed iterative fitting to determine the best astrometric solution with the `IRAF` tool `GEOMAP`, and used `IRAF`'s `GEOTRAN` to apply the resulting transformation (D. Tody 1986). The final uncertainty on the position was approximately 2 HST pixels. We selected a region of the environment and calculated the probability that a chance alignment occurs within a 2 pixel radius aperture to be 0.01%, indicating that the source is unlikely to be a chance coincidence.

Unfortunately, there was no unambiguous detection of SN 2021qvo, although there was a possible detection in F555W within the uncertainty interval of the best-fit position. Because SN 2021qvo is within the isophotal radius of its host galaxy, we measured the photometry from the cosmic-ray-corrected images within a 5 pixel radius using zero-points and aperture corrections provided by the WFC3 team.[22] For sky subtraction, we used the `photutils` package from

[22] https://www.stsci.edu/hst/instrumentation/wfc3/data-analysis/photometric-calibration/uvis-photometric-calibration

Table 3
Spectroscopic Observations of SN 2021qvo

UT Date	MJD (days)	Epoch[a] (days)	Telescope	Instrument
2021-06-23	59388.00	−13.2	NOT[b]	ALFOSC
2021-07-09	59404.40	3.2	Lick	KAST
2021-07-15	59410.16	9.0	Lick	KAST
2021-07-19	59414.82	13.6	Goodman	HST
2021-10-14	59501.01	99.8	Gemini-S	GMOS
2021-10-14	59501.06	99.9	Gemini-S	GMOS
2021-11-06	59524.00	122.8	Keck I	LRIS
2025-07-27[c]	60883.40	1482.2	Keck I	LRIS

Notes.
[a] Phase relative to rest-frame *B*-band maximum on MJD 59401.2.
[b] Nordic Optical Telescope
[c] Host-galaxy light only.

`AstroPy` to find pixels along the same elliptical isophote relative to the host-galaxy center of SN 2021qvo; we constructed an annulus around the host galaxy with a 10 pixel width to match the diameter of the photometric aperture.

Due to the lack of a galaxy template, we cannot be confident that we have detected the SN rather than galaxy flux; the measured magnitude of F555W = 26.25 ± 0.28 mag (AB) is insufficient to provide meaningful late-time CSM interaction constraints.

2.3. Spectroscopic Data and Redshift Determination

SN 2021qvo has seven epochs of spectroscopic data spanning ∼−13 days to ∼+123 days relative to maximum light (Table 3). Spectra were taken with ALFOSC, the Kast Double Spectrograph (J. S. Miller & R. P. S. Stone 1994), the Goodman High Throughput Spectrograph (J. C. Clemens et al. 2004), the Gemini Multi-Object Spectrograph (I. M. Hook et al. 2004), and the Low-Resolution Imaging Spectrometer (J. B. Oke et al. 1995). An additional host-galaxy spectrum was taken with LRIS on 2025 July 27. Table 3 logs the spectroscopic data for SN 2021qvo. The Kast and LRIS data were reduced using the UCSC Spectral Pipeline.[23] All spectra were corrected for bias, overscan, and flat-field frames. Wavelength calibrations used arc lamps acquired during the same night and the same instrument settings. When possible, the telluric bands were removed using standard star observations.

To determine the redshift from the final host-galaxy spectrum, we use the the `XCSAO` package (M. J. Kurtz et al. 1992). `XCSAO` compares spectra to a set of galaxy spectral templates and measures the best-fit cross correlation redshift; from the host-galaxy spectrum of SN 2021qvo, we find a precise redshift of 0.04205.

3. Host-galaxy Properties

We estimated the host-galaxy properties of SN 2021qvo using the `Blast` web application (D. O. Jones et al. 2024).[24] `Blast` estimates physical parameters of transient host galaxies by measuring photometry from Galaxy Evolution Explorer (D. C. Martin et al. 2005), SDSS (D. G. York et al. 2000; M. R. Blanton et al. 2017; R. Ahumada et al. 2020), Pan-STARRS (K. C. Chambers et al. 2016), DECam (A. Dey et al. 2019), Two Micron All Sky Survey (M. F. Skrutskie et al. 2006), and Wide-field Infrared Survey Explorer (E. L. Wright et al. 2010). `Blast` uses global host-galaxy apertures that are adjusted for the PSF of each individual filter/instrument to measure the photometry and fits to stellar population synthesis models via the Prospector-α model (J. Leja et al. 2017; B. D. Johnson et al. 2021), which is implemented via the SBI++ neural posterior estimator for increased speed (B. Wang et al. 2023).

The host galaxy of SN 2021qvo is faint, with PS1 $g \simeq 22.1$ mag, and is nearly coincident with the SN location, at (α, δ) of (22:08:12.11, +07:07:00.84). SN 2021qvo occurred in an unusually faint, low-mass host galaxy with a stellar mass $\log(M_*/M_\odot) = 7.83^{+0.17}_{-0.24}$ dex. Although this is less massive even than most reported 2003fg-like hosts, which prefer low-mass galaxies (C. Ashall et al. 2021; J. Lu et al. 2021), the host galaxy of at least one—SN 2022ilv—is even fainter (S. Srivastav et al. 2023). `Blast` also reports host-galaxy masses $\log(M_*/M_\odot) < 9$ dex for 2003fg-like SNe 2007if and iPTF13asv (see also R. A. Scalzo et al. 2010; Y. Cao et al. 2016b). While not highly star forming, there is an indication of recent star formation in the host of SN 2021qvo, with a global star formation rate of $\log_{10}(\mathrm{SFR}\ \ M_\odot\ \mathrm{yr}^{-1}) = -1.82^{+0.59}_{-0.78}$ and a global specific star formation rate $\log(\mathrm{sSFR}\ \ \mathrm{yr}^{-1}) = -9.70^{+0.82}_{-0.79}$. The host-galaxy dust is not well constrained by `Blast`, with the best-fit A_V consistent with ∼1–4 mag of extinction. The stellar metallicity is poorly constrained by the broadband photometry alone, but `Prospector` finds modest evidence that the host has a low metallicity, $\log(Z_*/Z_\odot) = -1.20^{+0.64}_{-0.47}$, which is typical of 2003fg-like SNe Ia and may imply low-metallicity progenitors (e.g., M. Childress et al. 2011; E. Y. Hsiao et al. 2020; C. Ashall et al. 2021; J. Lu et al. 2021).

Compared to the larger population of SNe, SN 2021qvo is relatively unique. It has a mass lower than 98.7% of SN Ia hosts measured by `Blast`, and 99.5% of transients overall; the comparison set includes 5408 spectroscopically classified SNe, of which 3943 are SNe Ia, and 8 have been classified as 2003fg-like. Its sSFR is somewhat less extreme; it is higher than 84% of SNe Ia and 81% of all transients. Lastly, SN 2021qvo's host-galaxy metallicity is lower than 87% of transient hosts measured by `Blast`, and 89% of SNe Ia.[25]

4. Photometry

In this section, we discuss the photometric properties of SN 2021qvo, including the light curve, the color-stretch parameter s_{BV}, the color curves, and the peak magnitudes, and compare them to other SN Ia subtypes. This analysis will help characterize the properties of SN 2021qvo and solidify it as a 2003fg-like SN event. The photometric data for SN 2021qvo are summarized in Tables 1 and 2.

[23] https://ucsc-spectral-pipeline.readthedocs.io/en/latest/
[24] https://blast.scimma.org/ with 2021qvo's results at https://blast.scimma.org/transients/2021qvo/.
[25] The comparison sample of `Blast` hosts is primarily sourced from magnitude-limited Transient Name Server discoveries, and we do not rigorously evaluate the selection effects in this work. If we restrict to blindly selected Transient Name Server (TNS) sourced transients, the results are nearly identical. While we have not fully vetted the individual `Blast` results for this comparison, the overall trends are reliable.

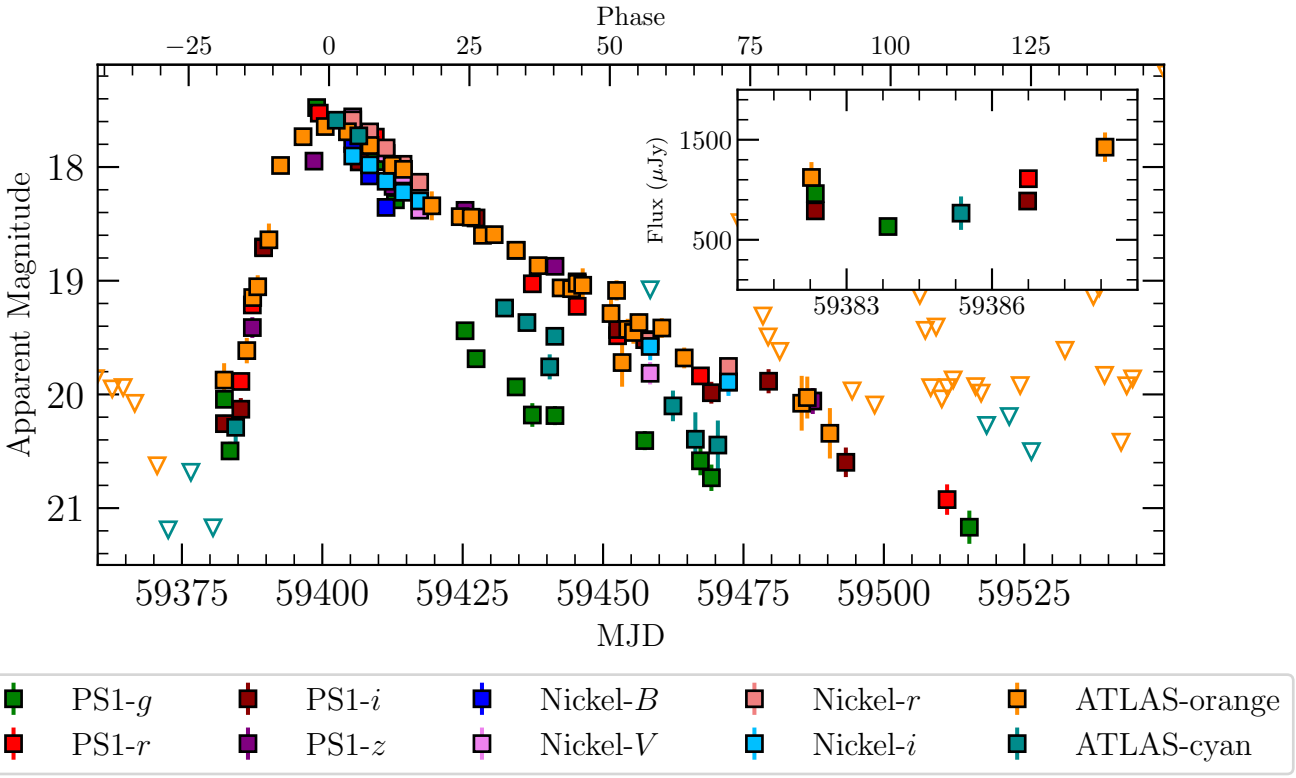

Figure 1. SN 2021qvo observations in different filters, plotted as days from the g-band peak (MJD = 59401.2) versus the observed magnitude. Downward-facing triangles denote upper limits. The inset shows a zoomed-in portion of the light curve in flux space from −20 to −15 days before peak, showing the early time light-curve bump.

4.1. Light Curves

Figure 1 shows the light curve of SN 2021qvo, with the inset showing the rising light-curve bump around 18.5 days before peak light. The bump is most clearly visible in the g band, with a $\sim 4.4\sigma$ detection of the decrease in flux. The i band also shows a signature attributable to a bump: a nearly flat light-curve evolution over a span of $\sim$3 days nearly 2 weeks before maximum light is highly atypical of all known SNe Ia. A natural explanation for the flat i-band light curve is that SN 2021qvo rises through or peaks at the first i-band detection, declines, and again rises through the second i-band detection. Alternatively, the light curve could be declining through the second point, but the later evolution requires it to rise again. Finally, the o-band light curve also exhibits a 4.7σ flux excess. Given the multiband signatures, especially in the g band, which is well above the YSE detection threshold, we conclude there is a highly significant rising light-curve bump in SN 2021qvo.

We next use the SuperNova in object-oriented Python (`SNooPy`) software (C. R. Burns et al. 2011, 2014) to determine the light-curve parameters of SN 2021qvo. The `SNooPy` package is designed to fit SN Ia photometry to an empirical light-curve model. Specifically, we use `SNooPy`'s `EBV_model2`, which fits the SN magnitudes, time of B-band maximum light, host-galaxy extinction, and a light-curve shape parameter that can be either the "color-stretch" parameter s_{BV}, the time difference between the B-band maximum and the reddest point in the $(B-V)$ color curve normalized by 30 days (C. R. Burns et al. 2014), or $\Delta m_{15}(B)$, the difference in B-band magnitude between the peak and 15 days after the peak (M. M. Phillips 1993). Here, we use s_{BV}, which is a more recent and improved stretch parameter (C. R. Burns et al. 2014); it also allows easy comparison to measurements from previous 2003fg-like samples (C. Ashall et al. 2021). The `SNooPy` fit to SN 2021qvo is shown in Figure 2; note that the `SNooPy` model assumes SN 2021qvo is a normal SN Ia and therefore predicts a secondary maximum in the i and z bands; however, secondary i- and z-band maxima are not present in 2003fg-like SNe Ia (S. Taubenberger 2017; C. Ashall et al. 2021).

To minimize errors resulting from the lack of 2003fg-like SN Ia fitting templates in `SNooPy`, we first used the built-in Gaussian process function to fit all our available bands with the early time bump masked out. We use these fits to set priors on the time of maximum light in the subsequent `EBV_model2` fits. SN 2021qvo peaks in the B band[26] on MJD = 59401.2 ± 1.00 days at $m_{g,\max} = 17.42 \pm 0.03$ mag and has a color-stretch parameter $s_{gr} = 1.210 \pm 0.116$ (using the linear correlation found by C. Ashall et al. 2020, we calculate an $s_{BV} = 1.184 \pm 0.121$). Correcting only for the redshift-derived distance, we estimate a g-band peak absolute magnitude of $M_{g,\max} = -19.3 \pm 0.249$ mag. This ranks SN 2021qvo among the lower-luminosity 2003fg-like SNe Ia such as SN 2012dn (N. K. Chakradhari et al. 2014) and SN 2022pul (M. R. Siebert et al. 2024).

4.2. Color Curves

Figure 3 shows the $g-r$ and $r-i$ color curves for SN 2021qvo and a comparison sample of other 2003fg-like

[26] While we do not have B-band photometry, `SNooPy` determines the time of peak in the B band by mangling the E. Y. Hsiao et al. (2007) spectral energy distribution (SED) to match the colors of SN 2021qvo. It then computes synthetic B-band light curves from the mangled SED.

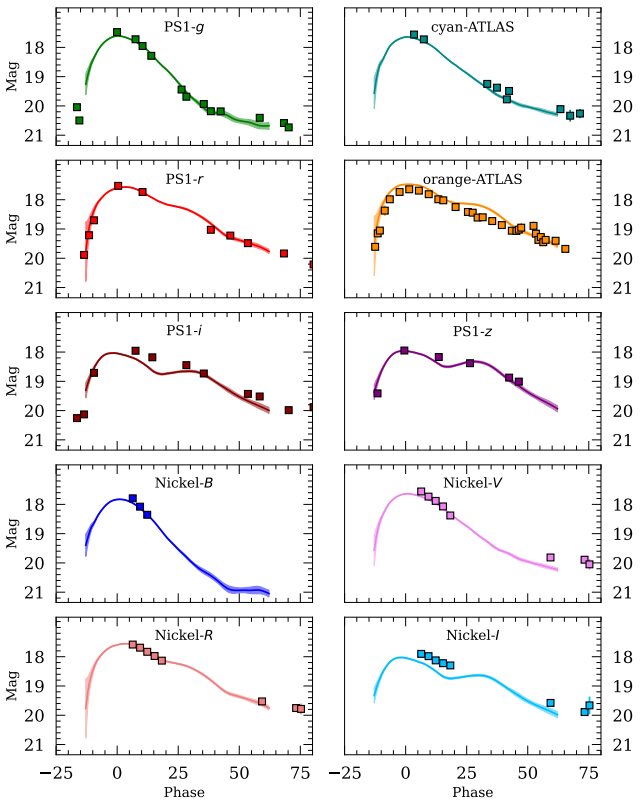

Figure 2. SNooPy fits for all 10 bands of SN 2021qvo. Plotted as time from *B*-band peak given by SNooPy versus the observed magnitude. Upper limits were removed when fitting the light curve.

SNe Ia from the Carnegie Supernova Project corrected for Milky Way extinction but without host-galaxy extinction correction. The comparison sample includes SNe 2007if (C. Akerlof et al. 2007), 2009dc (T. Puckett et al. 2009), LSQ12gqw (C. Baltay et al. 2013), 2013ao (C. Ashall et al. 2021), LSQ14fmg (C. Baltay et al. 2013), CSP14abk (C. Ashall et al. 2021), ASASSN-15hy (T. W. S. Holoien et al. 2015), and KISS15n (C. Ashall et al. 2021).

SN 2021qvo shows a color evolution consistent with other 2003fg-like SNe Ia. As detailed by C. Ashall et al. (2021), the $r-i$ curve demonstrates the greatest differences between individual 2003fg-like events in terms of their bluest point and color curve shape. Although the data are somewhat limited, SN 2021qvo is bluer in $r-i$ near the peak and appears to have larger color changes as a function of phase than other 2003fg-like SNe Ia, with the largest color difference being $\Delta(r-i)=0.49$ mag between the bluest and reddest point and a $\Delta(r-i)=0.11$ mag within 15 days at later epochs. This leads to the bluest point around 8 day post-*B*-band peak at $r-i=-0.33$ mag, similar to the bluest range of most other 2003fg-like SNe Ia and redder than normals (see Figure 9 in C. Ashall et al. 2021). We then see a flattening after the reddest point around ∼40 days until ∼80 days, consistent with other 2003fg-like events. After this, the large uncertainties make inferring the color evolution of SN 2021qvo tenuous.

The $g-r$ curve shows a prepeak evolution consistent with the early colors of KISS15n, starting around $g-r=0.01$ mag before reaching its bluest point ∼2 days before the peak. The curve then becomes redder like the other 2003fg-like SNe Ia in an almost monotonic nature. After reaching its reddest point at around 40 days, SN 2021qvo gradually becomes bluer at later

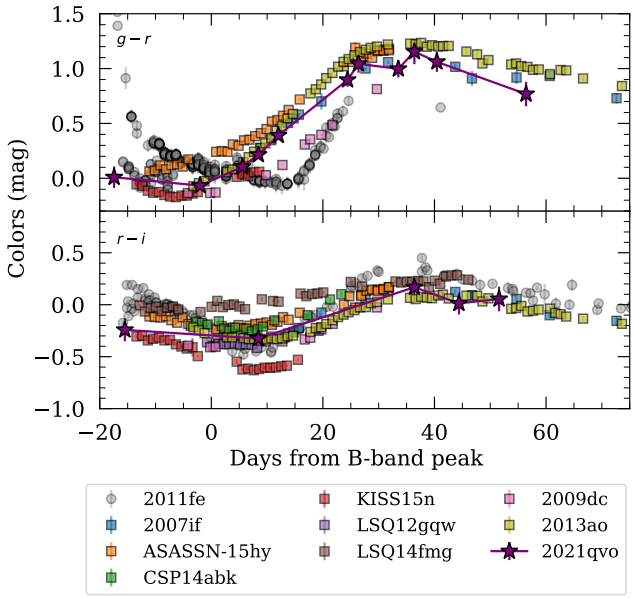

Figure 3. Color evolution plot for SN 2021qvo in the $r-i$ and $g-r$ bands. The data used are from the *g*, *r*, and *i* bands collected by Pan-STARRS. A comparison is made using other confirmed 2003fg-like SNe Ia derived from the Carnegie Supernova Project (C. Ashall et al. 2021), as well as a normal type SN Ia SN 2011fe. Curves were not corrected for host-galaxy extinction.

times. This continues until 80 days, when again, the large uncertainties prevent robust conclusions about the color evolution at later phases.

4.3. Luminosity-width Relation

The LWR (M. M. Phillips 1993) relates the light-curve shape of an SN Ia to its intrinsic luminosity. Normal SNe Ia have a tightly correlated LWR, with the more luminous SNe Ia having slower decline rates, and the less luminous SNe Ia having faster decline rates. 2003fg-like SNe Ia are often located on the luminous and broad area of the LWR parameter space. However, 2003fg-like SNe Ia span a variety of luminosities and light-curve shapes, including some extremely luminous events (e.g., SN 2007if, R. A. Scalzo et al. 2010; SN 2009dc, J. M. Silverman et al. 2011; S. Taubenberger et al. 2011; and LSQ14fmg, E. Y. Hsiao et al. 2020) and some underluminous events (relative to their light-curve shape, e.g., ASASSN-15hy, J. Lu et al. 2021).

Figure 4 shows SN 2021qvo on the *B*-band vs s_{BV} LWR diagram. We compare SN 2021qvo to normal SNe Ia from CSP-I (K. Krisciunas et al. 2017; C. R. Burns et al. 2018) and confirmed 2003fg-like SNe Ia from C. Ashall et al. (2021). The 2003fg-like sample includes SNe 2006gz (M. Hicken et al. 2007), 2007if (C. Akerlof et al. 2007), 2009dc (T. Puckett et al. 2009), 2012dn (N. K. Chakradhari et al. 2014), 2013ao (C. Ashall et al. 2021), LSQ14fmg (C. Baltay et al. 2013), ASASSN-15hy (T. W. S. Holoien et al. 2015), and ASASSN-15pz (P. Chen et al. 2019). Although it is the least luminous object in the sample, the location of SN 2021qvo on the LWR is coincident with the known sample of 2003fg-like SNe. SN 2021qvo is a notably underluminous 2003fg-like, instead blending into the normal SN Ia population rather than some of the more overluminous 2003fg-like SNe Ia. We note, however, a couple of reasons for this underluminosity. Due to the sparsity of our *B*-band data, SNooPy was unable to determine a *B*-band peak

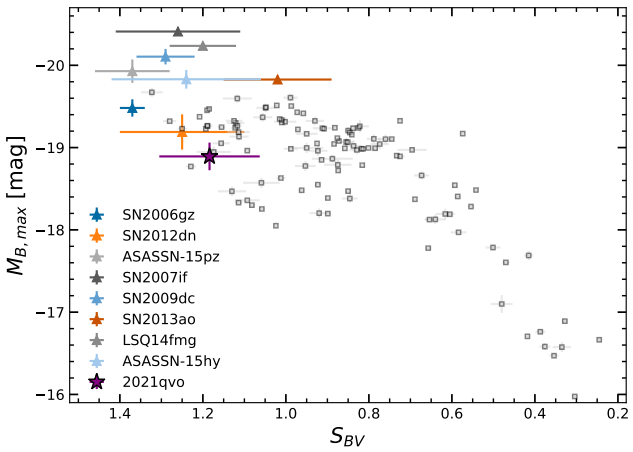

Figure 4. Luminosity-width relation, i.e., Phillips relation (M. M. Phillips et al. 1999), plot for SN 2021qvo and multiple 2003fg-like events, showing the relationship between the color-stretch parameter s_{BV} and the absolute magnitude in the B-band $M_{B,\max}$. The background sample of normal SNe Ia (gray squares) is taken from C. R. Burns et al. (2018). SN 2021qvo is shown as a purple star. We increased the error in SN 2021qvo's $M_{B,\max}$ to account for the sources of underluminosity detailed in Section 4.3. All other colored triangles are confirmed 2003fg-like events that have measurements in the B band. These events have been corrected for Milky Way extinction.

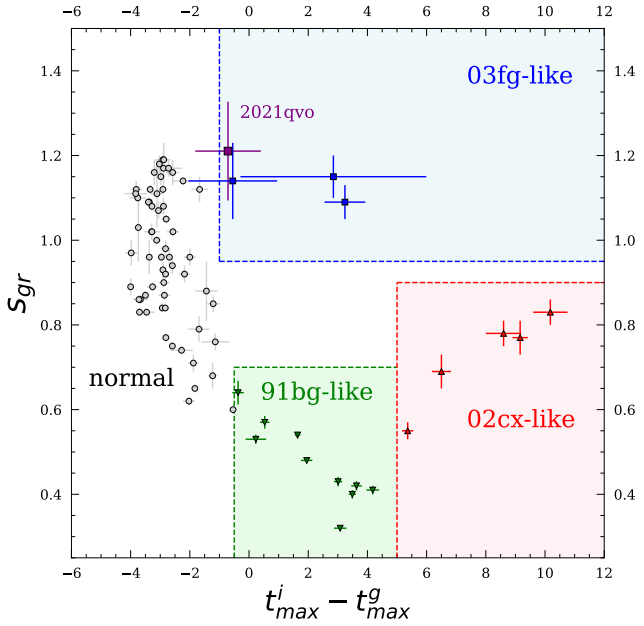

Figure 5. Color-stretch parameter s_{gr} as a function of the g-band maximum relative to the i-band maximum. SN 2021qvo (purple) can be seen in the top right. Approximate boxes are laid out to coincide with the classifications of different SN Ia subtypes (C. Ashall et al. 2020, 2003fg-like, 1991bg-like, and 2002cx-like SN Ia). Diagram derived from Figure 3 in C. Ashall et al. (2020).

absolute magnitude using a Gaussian process function, so we instead use the nearest data point as our estimate. This happens to be ~4 day postpeak, so we expect a peak B-band magnitude similar to SN 2012dn if accounting for this. Additionally, correcting for the relatively red color of SN 2021qvo (SNooPy finds a value of $E(B-V)_{\rm host} = 0.151 \pm 0.037$ mag) would increase its absolute magnitude by ~0.5–1 mag in Figure 4.

4.4. Photometric Subtype Identification

C. Ashall et al. (2020) presented a method to photometrically differentiate between subtypes using the color-stretch parameters, s_{BV} or s_{gr},[27] and the difference between the time of i-band maximum versus either the B-band or g-band maximum. The time at which the i-band peaks relative to other bands is the physical driver behind why this diagnostic works. It traces the speed of the recombination front of the Fe-group elements in the ejecta and, thus, the temperature evolution and adiabatic cooling rate. In particular, 1991bg-like, 2002cx-like, and 2003fg-like SNe Ia are easily identified in this parameter space because their i-band maximum occurs after their B-band or g-band maximum times. For more extensive discussion of this diagnostic, see C. Ashall et al. (2020).

Figure 5 shows s_{gr} versus the g- and i-band times of maximum ($t^i_{\rm max} - t^g_{\rm max}$), with SN 2021qvo located in the 2003fg-like SN Ia region. Of the 2003fg-like SNe Ia from this sample, SN 2021qvo has the smallest time difference between the g and i bands yet is still consistent with all other 2003fg-likes in the diagnostic, with i-band maximum coming ~0.7 days after the g-band maximum.

4.5. Characterizing the Early Time Bump

As summarized in W. B. Hoogendam et al. (2024), the rising light curves of SNe Ia can be categorized as one of "single power law," "double power law," and "bump." Most SNe Ia light curves fall under the "single" category, where the light-curve behavior is well fit by a single power law. In the case of "double" light curves, their best fits can be characterized by broken or two-component power laws. "Bump" cases have a nonmonotonic rising light curve, with a declining light curve within the timescales of ~1–4 days before rising again to maximum light. These bumps have been observed in the UV and optical for 2003fg-like SNe Ia (J.-a. Jiang et al. 2021; G. Dimitriadis et al. 2023; S. Srivastav et al. 2023) and 2002es-like SNe Ia (e.g., Y. Cao et al. 2016a; S. Srivastav et al. 2023).

A bump can be observed for SN 2021qvo in both the Pan-STARRS and ATLAS data. Plotting the data from both telescopes onto Figure 6 shows nonmonotonic behavior in the rise of the light curve; the g band has the strongest bump, but lack of data during the exponential rise makes it impossible to fit a single-band Gaussian+t^2 model similar to previous works (e.g., B. J. Shappee et al. 2018; G. Dimitriadis et al. 2019; A. A. Miller et al. 2020a;C. Ye et al. 2024; Q. Wang et al. 2024; W. B. Hoogendam et al. 2025a, 2025b). Beginning with an ATLAS o-band observation around 16 days from i-band peak, a decrease of nearly 0.8 mag occurs in g band within a day before the quick rise indicative of SN light curves.

5. Spectroscopy

The spectroscopic data available for SN 2021qvo include seven optical spectra taken between −13 and +123 days from maximum light. These spectra are listed in Table 3, and their normalized evolution are shown in Figure 7.

5.1. Spectral Line Measurements

To quantify the spectral evolution of SN 2021qvo, we measure velocities and pseudoequivalent widths (pEWs) for the most prominent spectral features. Both of these quantities

[27] The s_{gr} parameter is analogous to s_{BV} but uses $g-r$ instead of $B-V$.

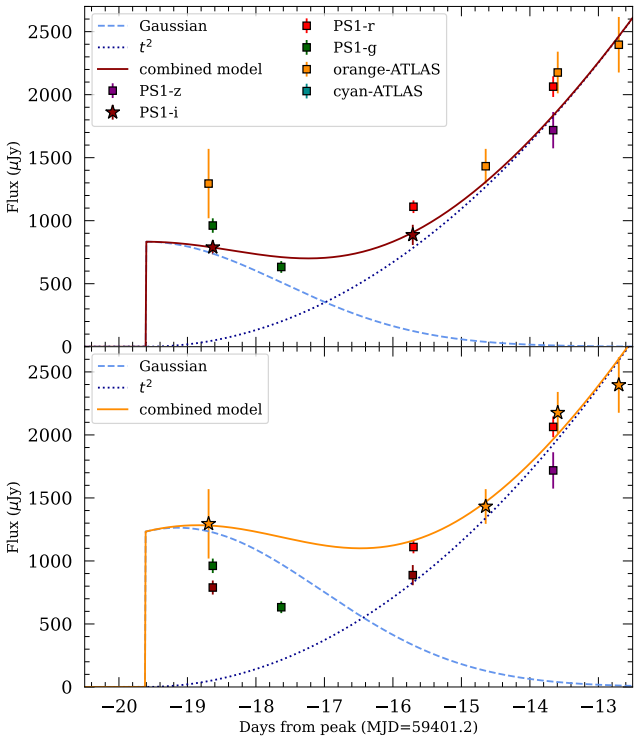

Figure 6. Flux-space light curve of the early time Pan-STARRS and ATLAS data for SN 2021qvo. For the *i* (top) and *c* (bottom) bands, the best-fit Gaussian (dashed) plus exponential t^2 rise (dotted) models, using the time of explosion determined by `MOSFiT` (Section 6.1), are plotted alongside the data. The star symbols indicate the filter fitted with the Gaussian model in each panel.

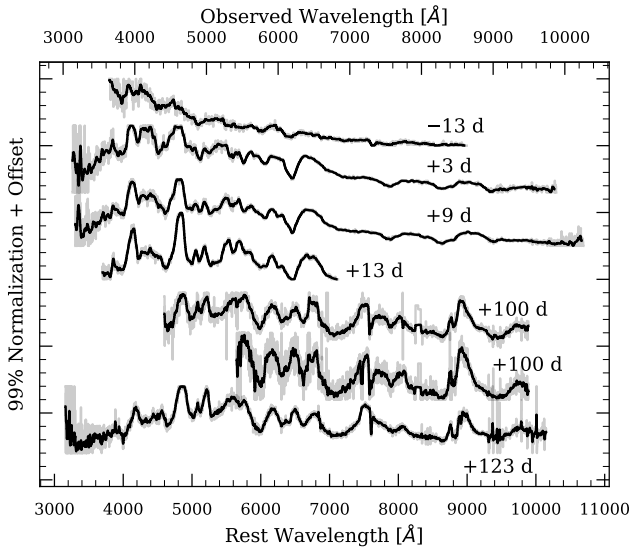

Figure 7. Spectral evolution of SN 2021qvo. Phases are from the best-fit SNooPy *B*-band peak (MJD 59401.2). Spectra have been normalized by using the range encompassing 99% of their flux to show features while accounting for the high noise data.

(The data used to create this figure are available in the online article.)

were extracted with the semiautomated line fitting `Python` program, Measure Intricate Spectral Features In Transient Spectra (`misfits`; S. Holmbo et al. 2023[28]) following the procedure in W. B. Hoogendam et al. (2022).

[28] https://github.com/sholmbo/misfits.

To derive the velocity of a feature, we used the `velocity.Gaussian` function, which determines a pseudocontinuum and then fits a Gaussian profile to the absorption feature, the minimum of which is taken as the velocity. We then use the `width.shallowpew` function to measure the pEW of a feature with the same pseudocontinuum, which integrates the absorption feature to extract a pEW (G. Garavini et al. 2007). Both of these functions estimate the respective uncertainties by computing 10,000 realizations using a Monte Carlo approach. The 1σ standard deviation of the posterior samples serves as the measurement's uncertainty. For both of these measurements, we employed the `lowpass` and `rawsmooth` arguments to remove high-frequency noise by passing the spectra through a low-pass filter to smooth them. Figure 8 shows SN 2021qvo's Si II spectral velocity and pEW evolutions derived from `misfits` in comparison to other 2003fg-like SNe and the median values of a normal SNe Ia catalog (M. R. Siebert et al. 2019). The comparative 2003fg-like sample is the same as in Figure 4 with the addition of SN LSQ12gpw (C. Baltay et al. 2013).

5.2. The Branch Diagram

D. Branch et al. (2006) found that the maximum light pEWs of the Si II λ5972 versus Si II λ6355 features differentiate SN Ia into four groups based on their spectral features: core normal, shallow Si, broad line, and cool. The "broad-line" SNe Ia have a broader Si II λ6355 feature than the "core normal" SNe Ia, perhaps indicating a high-velocity component. "Shallow silicon" SNe Ia have shallower Si II features, especially Si II λ5972. Lastly, "cool" SNe Ia have stronger Si II λ5972 features due to lower temperatures than core-normal SNe Ia.

Like most 2003fg-like SNe Ia (C. Ashall et al. 2021), SN 2021qvo is located in the shallow Si region of the Branch diagram (Figure 9). The Si II λ5972 pEW feature for SN 2021qvo is near the average of all 2003fg-like SNe. In contrast, the pEW of the Si II λ6355 feature is unusually low compared to other 2003fg-like SNe Ia events. This could indicate a higher explosion energy for SN 2021qvo, which may doubly ionize Si and produce Si III features instead of Si II. Only the extremely overluminous SN 2007if ($M_V = -20.4$ mag; R. A. Scalzo et al. 2010) has a lower Si II λ6355 pEW than SN 2021qvo.

5.3. Spectral Comparison

We compare SN 2021qvo to prepeak and postpeak spectra from other notable SNe Ia in Figures 10 and 11. Figure 10 compares the ~ -13 day spectrum of SN 2021qvo to four other SNe Ia with similarly early spectra. Around -11 days, the Si II λ6355 feature in the 2003fg-like SNe Ia (SNe 2009dc and SN 2021qvo) is present, in contrast to other overluminous subtypes such as 1991T and 1999aa-likes where weak Si II features appear after -7 days (e.g., M. M. Phillips et al. 2024). Compared to SN 2009dc, SN 2021qvo has a stronger Si II λ6355 feature but lacks the prominent C II λ6580 feature seen in SN 2009dc. In contrast to SN 2011fe, a canonically normal SN Ia with strong Si II $\lambda\lambda$5972, 6355 features, the rest of the sample has considerably shallower Si II double line features, a trait consistent with the prepeak and near-peak spectral behavior of these overluminous subtypes (see Figure 9).

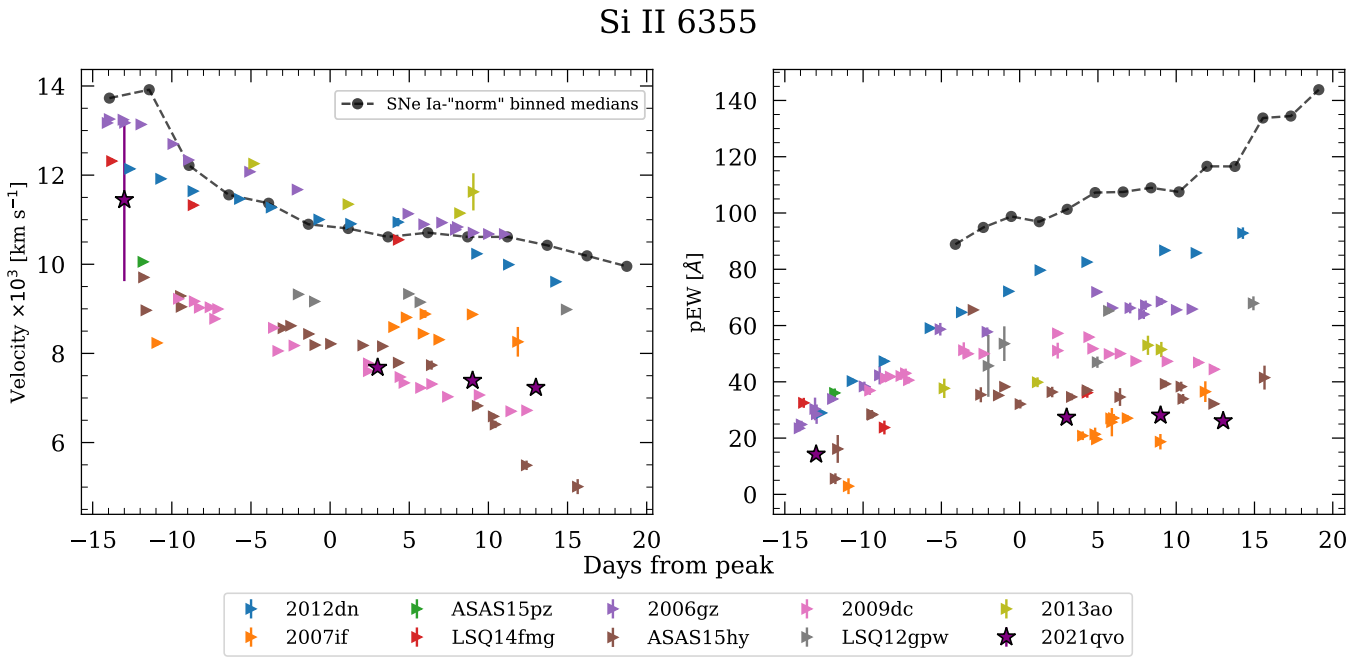

Figure 8. Velocity (left) and pseudoequivalent width (right) of the Si II λ6355 feature from SN 2021qvo's spectral data. The pEW and velocity evolutions for other 2003fg-like SNe from the Carnegie Supernova Project catalog (C. Ashall et al. 2021) are also plotted for comparison. Also plotted in black circles are the binned medians of the normal SNe catalog from M. R. Siebert et al. (2019).

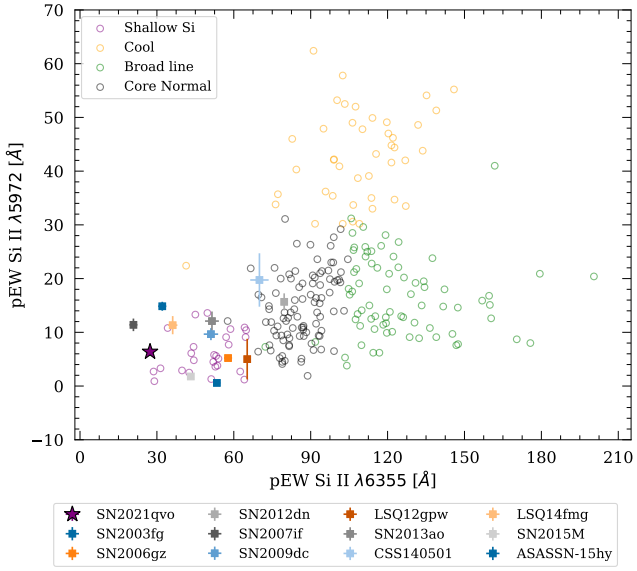

Figure 9. Branch diagram comparing the pEW of Si II λ5972 versus Si II λ6355. The hollow circles represent normal SN Ia, with the different colors corresponding to the four groups defined by D. Branch et al. (2006). Most 2003fg-like SNe Ia, including SN 2021qvo, are in the shallow Si region. Data for the 2003fg-like SNe was taken from C. Ashall et al. (2021), which includes the SNe samples from Figures 4 and 8 as well as SNe 2003fg (D. A. Howell et al. 2006), CSS140501 (A. J. Drake et al. 2009), and 2015M (T. Morokuma et al. 2015). The normal SNe Ia from S. Blondin et al. (2012), G. Folatelli et al. (2013), and W. B. Hoogendam et al. (2022).

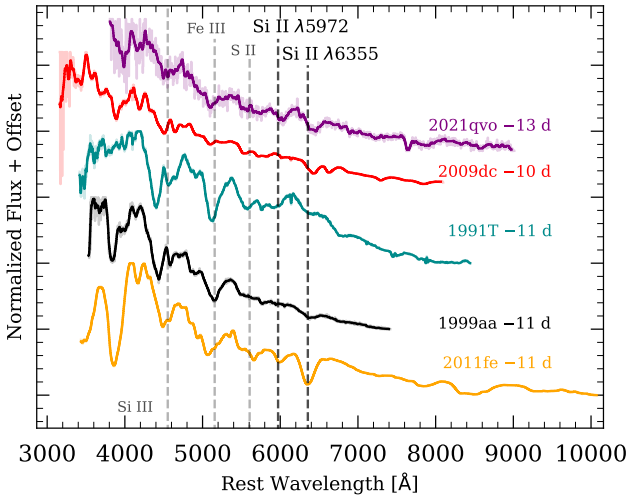

Figure 10. Spectral comparisons to SN 2021qvo at −13 days before maximum light. We show spectra from another 2003fg-like event, SN 2009dc, as well as a normal SN Ia and the notable 1991T and 1999aa subtypes around the same prepeak epoch. The two notable Si II features are highlighted. Other prominent features in the spectra are also labeled (Si III, Fe III, S II).

Figure 11 compares SN 2021qvo to the same SNe Ia as Figure 10 at ∼13 day postpeak. While these SNe Ia have spectra that significantly differ at −13 to −10 days, by +13 to +15 days, they are mostly similar (C. Ashall et al. 2021). This is due to the dispersion of the outer layers in these later days, leading to the recession of the photosphere well into the ^{56}Ni region. ^{56}Ni and its products then influence much of the spectra regardless of the subtype, resulting in spectral similarities at these later epochs.

One difference in the ∼15 day postpeak spectra may be in the line profile in the 5200 to 5400 Å region. SNe 2009dc and 2021qvo have two distinct peaks, whereas SNe 1991T and 1999aa have one peak and a blended decline, and SN 2011fe has a protruding knee feature. A detailed abundance tomography is beyond the scope of this work, but a population-level comparison of 2003fg-like SNe Ia and other normal and overluminous SNe Ia to understand the 5200–5400 region may reveal new insights into the explosion symmetry (perhaps these profiles arise from ejecta asymmetries that can be more easily seen in the NIR; J. O'Hora et al. 2025), physics

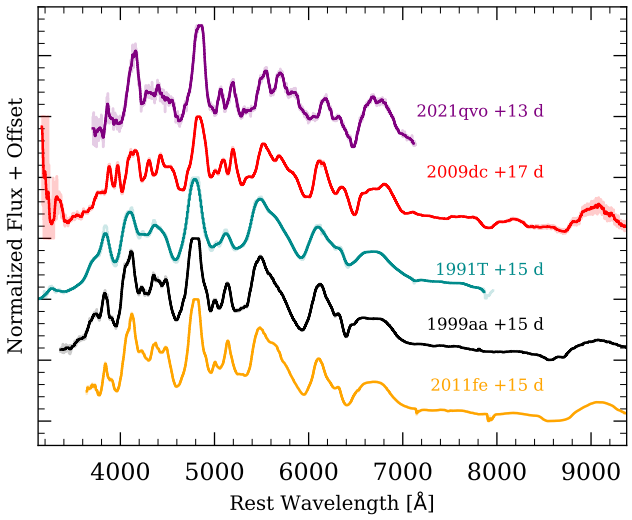

Figure 11. Spectral comparisons to SN 2021qvo at +13 days after maximum light. We show spectra from another 2003fg-like event, SN 2009dc, as well as a normal SN Ia and the notable 1991T and 1999aa subtypes around the same prepeak epoch.

(differences in burning may produce different elemental distributions), or temperature (resulting in different ionization fractions).

6. Constraints and Comparison of CSM in 2003fg-like SNe Ia

In this section, we constrain the explosion parameters of SN 2021qvo, including CSM interaction. We then examine our results alongside the CSM parameter constraints of other comparable 2003fg-like SNe in the literature.

6.1. Constraining CSM Interaction

We use the Modular Open Source Fitter for Transients (MOSFiT) to model SN 2021qvo (J. Guillochon et al. 2018). MOSFiT is a Python-based package that fits transient data to determine parameter distributions using Monte Carlo methods. Within MOSFiT, we use the built-in csmni model, which uses the CSM–ejecta (E. Chatzopoulos et al. 2013) and ^{56}Ni-Co radioactive decay (D. K. Nadyozhin 1994) models to fit the light curve of SN 2021qvo. In our modeling, we infer parameters by assuming that the early time bump is due to CSM interaction, although see Section 6.3 for an additional discussion.

The csmni model assumes that both ejecta–CSM interaction and ^{56}Ni decay contribute to the luminosity of the SN Ia. A dense CSM may form through mass loss of the progenitor WD (I. Hachisu et al. 2008), leftover material from the WD's main-sequence stage (D. Tsebrenko & N. Soker 2015), or donor material from a companion star (T. J. Moriya et al. 2019). Once the progenitor WD undergoes an SN Ia explosion, the SN ejecta interacts with the CSM, resulting in two shock waves, one moving back into the ejecta and the other carrying energy and the CSM outwards. These shocks then ionize the expanding material, resulting in detectable emission and a contribution to the SN luminosity. Such a model may explain overluminous SNe Ia by attributing the additional luminosity to CSM interaction (R. A. Chevalier 1982; R. A. Chevalier & C. Fransson 1994; E. Chatzopoulos et al. 2013).

For ^{56}Ni and the subsequent ^{56}Co decay emission, the primary power source of the SN light curve, the model assumes centrally concentrated ^{56}Ni. As the WD explodes, the ^{56}Ni near the core expands outward with the SN ejecta. The ^{56}Ni then decays to ^{56}Co, releasing high-energy photons absorbed by the ejecta and reemitted at lower energies. This primarily powers the observed light curve's peak luminosity and quick rise. The remaining ^{56}Co then further decays to stable ^{56}Fe, releasing more photons that power the later phases of the SN (E. Chatzopoulos et al. 2012). This ^{56}Ni scenario models most normal SN Ia well and leads to the W. D. Arnett (1982) relation that can be used to estimate ^{56}Ni mass (e.g., M. Stritzinger et al. 2006).

At early times, the CSM interaction may produce a significant fraction of the flux; thus, MOSFiT's csmni combination model can account for early time excess fluxes (see also SN 2022ywc; S. Srivastav et al. 2023). Its constituent CSM interaction and ^{56}Ni and ^{56}Co decay models are built from E. Chatzopoulos et al. (2013) and D. K. Nadyozhin (1994), respectively. MOSFiT's csmni model uses 10 free parameters: total ejecta mass ($M_{\rm ej}$), the fraction of ^{56}Ni mass with respect to total ejecta mass ($f_{\rm Ni} = \frac{M_{\rm Ni}}{M_{\rm ej}}$), kinetic energy ($E_k$), mass of the CSM shell ($M_{\rm CSM}$), inner radius of CSM shell (R_0), CSM density at the inner radius R_0 (ρ_0), time of the explosion relative to first observation ($t_{\rm exp}$), minimum temperature ($T_{\rm min}$), host-galaxy extinction ($A_V^{\rm host}$), and white noise variance (σ), a variable added to measurement uncertainties to allow additional unmodeled errors (J. Guillochon et al. 2018).

We apply a conservative upper bound on ρ_0, as it is not well constrained by the data. We compute the maximum value of ρ_0 assuming electron opacity from Thomson scattering and MOSFiT's quadratic power-law density profile. For a maximum optical depth of $\tau = 5$—above which essentially no photons could escape without interaction—and a hydrogen CSM, this gives a maximum density of $\rho = 6 \times 10^{-8}$ g cm^{-3} when assuming a minimum CSM radius of 2000 km (approximately equal to the surface of a high-mass WD; I. Caiazzo et al. 2021).

Our other priors follow S. Srivastav et al. (2023, their Table 1) with only a few minor differences. Primarily, R_0 and $M_{\rm CSM}$ are slightly more conservative in this analysis; we use a lower limit on R_0 of 2000 km and a lower limit on $M_{\rm CSM}$ of $10^{-7} M_\odot$. Additionally, the lower bound on $T_{\rm min}$ is 2000 K instead of 100 K, E_k spans from 0.01×10^{51} erg to 4×10^{51} erg (slightly more conservative), and M_{ej} has a higher maximum of $10 M_\odot$. We also use the host-galaxy redshift of $z = 0.04205$ to derive the distance; the luminosity distance assumes a flat ΛCDM model with $\Omega_m = 0.3$, $\Omega_\Lambda = 0.7$, and $H_0 = 70$ km s^{-1} Mpc^{-1}. Although not all parameters are well constrained by our limited data, our conservative choice in priors ensures that uncertainties are propagated accurately to the parameters of interest.

Lastly, because our initial fitting resulted in poor fits to the light curves after the peak, we use an integrated light curve to fit the later-time data. We found that MOSFiT's best fit to the full dataset initially used CSM interaction to fit the near-peak light curve, in an attempt to rectify discrepancies of up to ∼1 mag in the colors near maximum light, while leaving the early time bump unmodeled. For this reason, we fit the full light curve up to −5 days relative to the peak, and, for the later-time data, we use SNooPy to integrate fluxes with

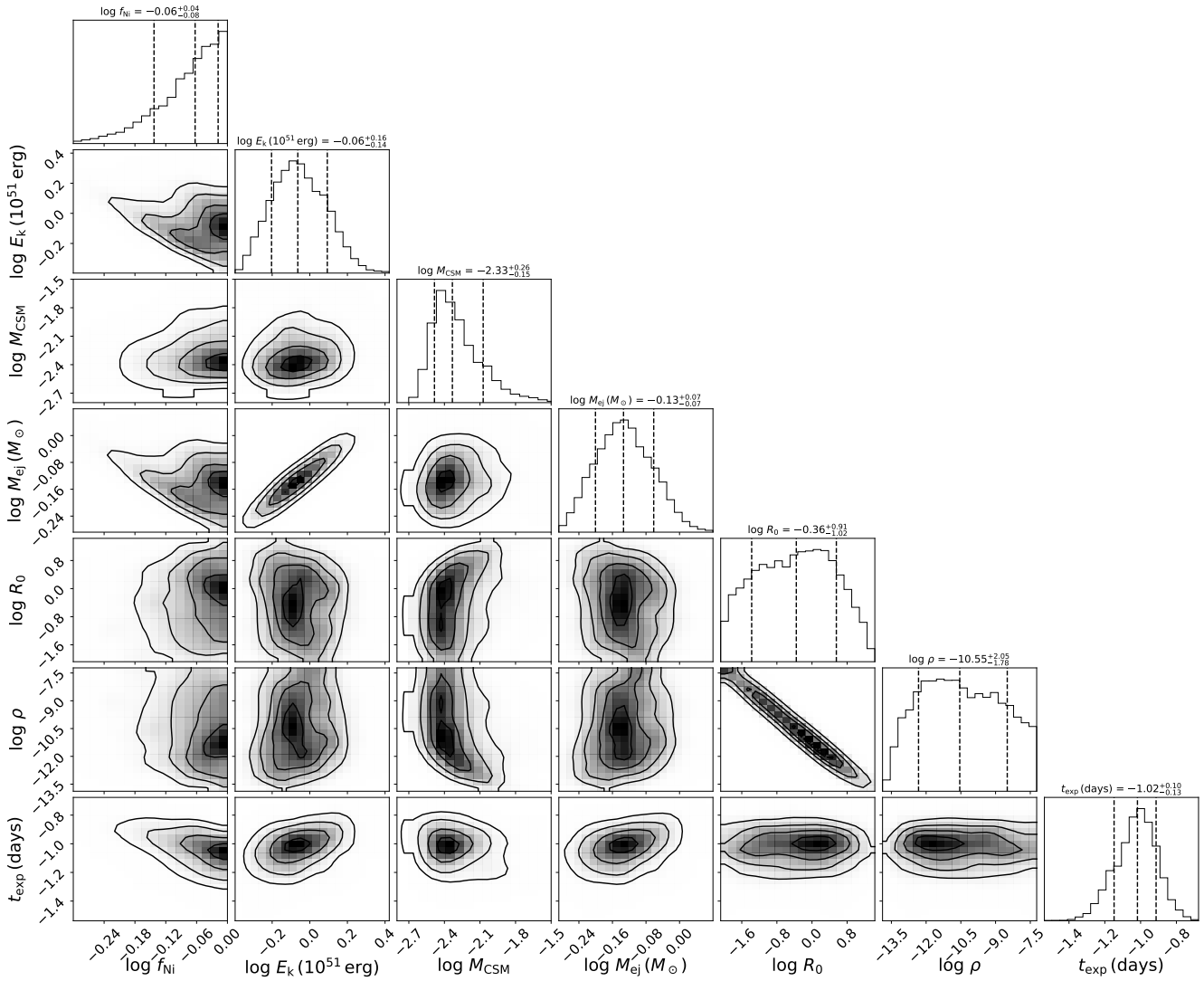

Figure 12. Corner plot of the parameter estimation for the MOSFiT csmni model. Parameter constraints (1σ) are shown above the histogram panels on the right-hand side. See text for explanation of the MOSFiT parameters.

Gaussian process interpolation across the optical bandpasses to produce an integrated optical light curve across (approximately) the *griz* bands and spanning ~ -5 to $+45$ days relative to the peak.[29] The early time data therefore constrain MOSFiT's CSM model, while the later-time light curve constrains MOSFiT's default model, which assumes the average light curve is powered by ^{56}Ni and ^{56}Co decay.

Our results from MOSFiT using 20,000 Markov Chain Monte Carlo steps—to ensure full sampling of the posterior—are shown in Figure 12. Although we have significant degeneracies, particularly between the density, the CSM mass, and the radius at which the CSM begins (e.g., a closer-in CSM and higher density produce similar light curves to farther-out CSM and lower density), we find that nonzero CSM mass best explains the observed light curves (Figure 13).[30] MOSFiT prefers CSM beginning at $\sim$0.05–4 AU, with a best-fit mass of $\log_{10}(M_{CSM}/M_\odot) = -2.33^{+0.26}_{-0.15}$. There is also a long, low-probability tail to CSM masses of up to $\sim 0.03 M_\odot$ that is not fully ruled out by our data. We note that using a less-conservative density prior, such as $\rho = 10^{-11}$ g cm^{-3} following S. Srivastav et al. (2023), changes the mean CSM mass by just 0.09 dex, well within the errors.

We omit the extinction, minimum temperature, and white-noise variance from Figure 12 for visual clarity. The host-galaxy extinction is constrained to $\lesssim$0.4 mag at the 1σ level, using priors that range from 0 to 5.6 mag following S. Srivastav et al. (2023). The minimum temperature is $\log_{10}(T_{min}\ \ K) = 3.85^{+0.05}_{-0.16}$; however, it has a bimodal distribution with peaks at $\sim$3.7 and $\sim$3.9 dex. Lastly, the variance suggests an added model (or data) uncertainty of $\sim$0.08 mag is needed for a reduced $\chi^2 \simeq 1$.

6.2. Fitting Variants

While the MOSFiT fitting results are largely consistent with previous work (see Section 6.3 below), we derive an unphysical ^{56}Ni fraction near 1.0; this is likely because the ^{56}Ni model is not always a good approximation to the colors of 2003fg-like SNe Ia. This high ^{56}Ni fraction is driven by the

[29] This procedure uses SNooPy's bolometric luminosity computation tool, but here, we do not subtract the distance modulus or correct for host-galaxy extinction. We express the integrated quantities in AB magnitudes.

[30] Note that in SN 2022ywc this degeneracy is less pronounced (S. Srivastav et al. 2023), and therefore is likely due to our limited data around the time of CSM interaction.

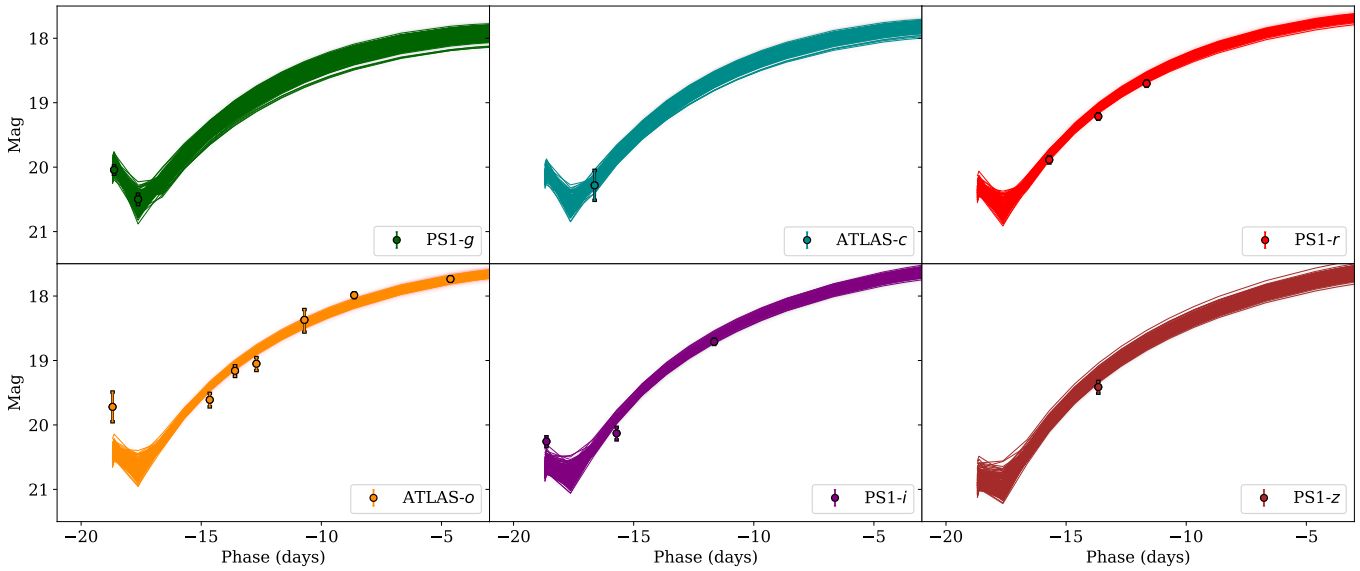

Figure 13. MOSFiT CSM+Ni model fitting on the six photometric bands available for SN 2021qvo. A bump is observed in the model within the first ∼2 days, corresponding to the early time bump seen in our data. We fit the premaximum light photometry up to −5 days and use an integrated optical bandpass at later times to constrain the ^{56}Ni decay (see text). We note that the postpeak model deviates significantly from the observed colors of SN 2021qvo, as discussed in the text; however, alternate fitting approaches yield consistent CSM parameters.

near-peak and later-time light curve; excluding the early data for SN 2021qvo does not significantly affect our measurement. Although fitting the later-time light curves is not the primary goal of this analysis, we perform two additional tests to ensure the robustness of our CSM mass estimates. First, we fit *only* the prepeak light curve, finding that the csmni model can match the early colors well and returns a consistent (0.9σ) best fit of $\log_{10}(M_{\rm CSM}/M_{\odot}) = -1.85^{+1.022}_{-0.46}$.

Second, we use SnooPy's integrated light curve computed from −5 to +45 days with MOSFiT's default model, which assumes the light curve is powered by ^{56}Ni and ^{56}Co decay, to derive the ^{56}Ni fraction. This yields a constraint on the ^{56}Ni fraction between 0.53 and 0.65, which we then use as a flat prior in the prepeak, multicolor light-curve fit. We note that the bolometric fit alone yields a slightly higher ejecta mass of $\sim 0.87^{+0.15}_{-0.09}$ $M_{\odot}$, but it is consistent with the baseline results at $\sim 1\sigma$ significance. From this analysis, we find $\log_{10}(M_{\rm CSM}/M_{\odot}) = -1.66^{+1.04}_{-0.72}$, again consistent with the unconstrained fit and demonstrating that the ^{56}Ni fraction and CSM mass are not strongly correlated and can be constrained independently (Figure 12). We treat the MOSFiT parameter estimation discussed in Section 6.1 as our baseline result, but note that the early time results alone may favor a slightly higher CSM mass.

As a third test, we fix M_{ej} to the Chandrasekhar mass to control for potential model degeneracies in ejecta mass when using the early time light curve. We find only a minimal change to the CSM mass, with a derived value of $\log_{10}(M_{\rm CSM}/M_{\odot}) = -2.26^{+0.42}_{-0.20}$ that differs from our baseline results by only 0.07 dex. This is further evidence that the derived CSM mass is not highly sensitive to uncertainties in the ejecta mass.

Lastly, including possible HST detections at late times does not significantly change the fit, with CSM masses on the order 10^{-2} remaining the best-fit solution. The late-time epochs are therefore consistent with a normally declining Ni^{56}-powered light curve.

As an independent check on the high ^{56}Ni fraction, we also measure the ^{56}Ni mass and total ejecta mass from the D. K. Khatami & D. N. Kasen (2019) model following the procedure in G. Dimitriadis et al. (2023). We adopt the same parameters as G. Dimitriadis et al. (2023), including a constant opacity of $\kappa = 0.1$ cm^2 g^{-1} and a value of $\beta = 1.6$ (a dimensionless constant) as suggested by Table 6 of D. K. Khatami & D. N. Kasen (2019). We estimate the peak luminosity of SN 2021qvo with extrabol as 2.706×10^{43} erg s^{-1} (I. Thornton et al. 2024) and adopt the best-fit time from the explosion to maximum light determined by MOSFiT of −19.6 days.

From this model, we derive a ^{56}Ni mass of $1.78 M_{\odot}$ and an ejecta mass of $1.89 M_{\odot}$ (higher than the best-fit MOSFiT ejecta mass of $0.75 M_{\odot}$), for a ^{56}Ni fraction of 0.94. We note that we derive ^{56}Ni fractions of greater than or nearly one for other 2003fg-like SNe; for SN 2021zny, we measure a ^{56}Ni fraction of 1.8,[31] for SN 2009dc, we find a ^{56}Ni fraction of 1.6, and for SN 2012dn, we find a ^{56}Ni fraction of 0.97. In practice, this may mean that bright and slow-evolving transients like 2003fg-like SNe Ia require an additional power source beyond ^{56}Ni to explain their luminosities. We leave a more in-depth analysis of this topic for future work.

6.3. Comparison to Other Rising Light-curve Bump Type Ia Supernovae

SN 2021qvo is another SN Ia with a nonmonotonic, rising light-curve bump and is one of fewer than 10 SNe Ia to have such a feature. It is just the fourth rising light-curve bump SN Ia with CSM mass estimates. Previous SNe Ia with rising light-curve bumps include iPTF14atg (Y. Cao et al. 2015; M. Kromer et al. 2016), SN 2019yvq (A. A. Miller et al. 2020b; J. Burke et al. 2021; M. A. Tucker et al. 2021), SN 2020hvf (J.-a. Jiang et al. 2021), SN 2021zny (G. Dimitriadis et al. 2023; although this claim has been disputed by M. M. Fausnaugh et al. 2023), SN 2022ilv (S. Srivastav et al. 2023), and the 2002es-like SN 2022ywc (S. Srivastav

[31] We find a small error in the ^{56}Ni mass calculation of G. Dimitriadis et al. (2023) that results in a significantly increased value.

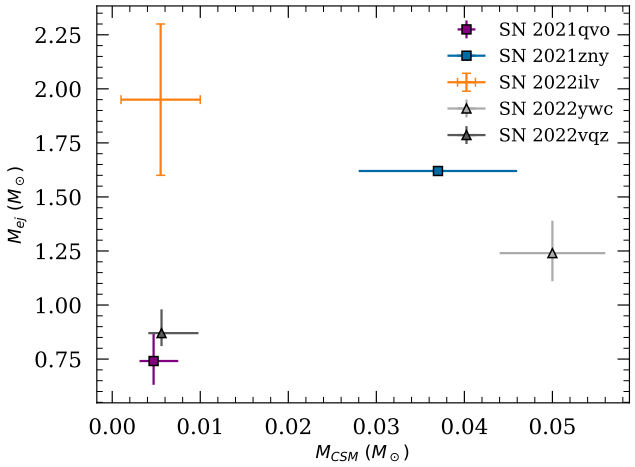

Figure 14. Estimated CSM mass versus SN ejecta mass for early time bump SNe Ia with CSM mass estimates. Here, we plot the values for SN 2021qvo from our `MOSFiT csmni` results in Section 6.1. SNe plotted with square markers represent 2003fg-like events, and the triangle marker indicates a 2002es-like SNe. SN 2022ilv is an 2003fg-like SNe plotted solely with error bars due to S. Srivastav et al. (2023) calculating estimated ranges for both the CSM and ejecta masses (S. Srivastav et al. 2023 used the `SuperBol` code; from M. Nicholl 2018 to model the bolometric light curves of SN 2022ilv, then employed the Arnett model to estimate the explosion parameters). Additionally, SN 2021zny lacks uncertainty in the ejecta mass as G. Dimitriadis et al. (2023) fixed the value for their estimates.

et al. 2023). We also note that SN 2022pul, although lacking early time coverage, has nebular-phase data that are consistent with expectations from a CSM–ejecta interaction progenitor model (M. R. Siebert et al. 2024).

The existing samples of early time bump SNe Ia all have CSM mass estimates of the order 10^{-2} to $10^{-3} M_\odot$. SN 2022ilv (S. Srivastav et al. 2023) had an estimated $M_{\rm CSM} \simeq 10^{-2}$ to $10^{-3} M_\odot$ of material, while SN 2022ywc had $0.050 \pm 0.006 M_\odot$ (which had a much stronger and longer-duration bump; S. Srivastav et al. 2023). SN 2021zny had a best-fit 0.04 $M_\odot$ of material (G. Dimitriadis et al. 2023). Our best-fit CSM mass is fully consistent with the mass range from these previous analyses (Figure 14).

Of these early time bump SNe, only SNe 2022ywc and 2022vqz (G. Xi et al. 2024), both 2002es-like SNe, have been fit with the `MOSFiT` CSM+Ni model. Overall, while SN 2022ywc has a much stronger shock-cooling signature than 2021qvo, reaching an absolute magnitude of ~ -19 in the ATLAS o band, we find that the physical parameters of SN 2021qvo are broadly consistent within the uncertainties. Specifically, our ejecta mass, $\sim 0.74 M_\odot$, is $\sim 2.7\sigma$ lower than SN 2022ywc ($\sim 1.24 M_\odot$), while our explosion energy is consistent within 1σ. The CSM density is somewhat higher but just at $\sim 1.2\sigma$ significance; we emphasize that our measurement from SN 2021qvo is extremely uncertain. The best-fit CSM radius in SN 2021qvo is also consistent with SN 2022ywc, and it is degenerate with CSM mass and density. SN 2022vqz, which has a relative bump strength that is much more consistent with SN 2021qvo, also has CSM masses that are consistent with SN 2021qvo within the uncertainties ($(M_{\rm CSM}/M_\odot) = 5.6^{+4.2}_{-1.5} \times 10^{-3}$) and a slightly higher ejecta mass of $\sim 0.87^{+0.11}_{-0.06}$ $M_\odot$.

Previous studies have examined alternative explanations for early time excesses, including bumps, in SNe Ia. These models include surface He-detonations (e.g., K. Maeda et al. 2018; A. Polin et al. 2019), surface ^{56}Ni mixing (e.g., A. L. Piro & V. S. Morozova 2016; M. R. Magee et al. 2020), and nondegenerate companion interaction (e.g., D. Kasen 2010; K. Maeda et al. 2014). However, each of these models has challenges to explain the observations, in particular, the blue UV colors and occurrence rates (see W. B. Hoogendam et al. 2024, for further discussion). To date, the existing 2003fg-like events with observed light-curve bumps paint a consistent picture of CSM around their progenitor systems, with future statistical samples and fitting methods (e.g., N. Sarin et al. 2024) likely to enable additional tests of this model.

7. Summary

In this manuscript, we present SN 2021qvo, one of a growing class of 2003fg-like SNe Ia with bumps in their early time light-curve flux. We analyze photometric data from YSE and ATLAS beginning nearly 17 days before the peak, plus an optical spectroscopic time series spanning -13 to $+123$ days relative to maximum light.

SN 2021qvo occurred in a low-mass dwarf galaxy with $\log(M_*/M_\odot) = 7.83^{+0.17}_{-0.24}$ dex and has evidence for low stellar metallicity, characteristic of other known 2003fg-like host galaxies. Our analysis of the light-curve shape, luminosity, and Si II pEW and velocities indicates that SN 2021qvo is fully consistent with the 2003fg-like subtype.

After classifying SN 2021qvo, we test the leading progenitor theory for overluminous SNe Ia with an early time bump, CSM–ejecta interaction. We use the `MOSFiTcsmni` model to estimate the interaction of ejecta with CSM in the early time light curve, finding a best-fit CSM mass of $\log_{10}(M_{\rm CSM}/M_\odot) = -2.33^{+0.26}_{-0.15}$, which is in broad agreement with constraints from other 2003fg-like SNe Ia in the literature. Despite being unable to constrain degeneracies between density and radius fully, we find significant evidence for a nonzero CSM to explain the early time observed bump.

SN 2021qvo is the latest example of a 2003fg-like SN Ia with a rising light-curve bump. The origin of these nonmonotonic bumps, which have only been seen in 2002es-like and 2003fg-like SNe Ia (W. B. Hoogendam et al. 2024), remains intriguing. Recent observational analyses (e.g., C. Ashall et al. 2021; W. B. Hoogendam et al. 2024) have found the most likely explanation to be SN ejecta interacting with CSM, but the origin of this CSM is not yet well constrained. Possible explanations include an asymptotic giant branch (AGB) stellar envelope that has lost most if not all of its H and He (A. Kashi & N. Soker 2011; M. Ilkov & N. Soker 2013; N. Soker & E. Bear 2023), or from ejected CO during the merger event of two WDs (K. J. Shen et al. 2012; N. Levanon et al. 2015). As the number of SNe Ia with rising light-curve bumps increases due to continued early time discovery, classification, and follow-up efforts, our understanding of the properties and origin of this plausible enshrouding material will improve.

Acknowledgments

We thank Nikhil Sarin for helpful discussions.

I.A.A.P. acknowledges support from the Research Experience for Undergraduates program at the Institute for Astronomy, University of Hawai'i, funded through NSF grant No. 2050710, and would like to thank the Institute for Astronomy for their hospitality during the course of this project. W.B.H. acknowledges support from the National

Science Foundation Graduate Research Fellowship Program under grant Nos. 1842402 and 2236415. Any opinions, findings, conclusions, or recommendations expressed in this material are those of the author(s) and do not necessarily reflect the views of the National Science Foundation. D.O.J. acknowledges support from NSF grants AST-2407632 and AST-2429450, NASA grant 80NSSC24M0023, and HST/JWST grants HST-GO-17128.028, HST-GO-16269.012, and JWST-GO-05324.031, awarded by the Space Telescope Science Institute (STScI), which is operated by the Association of Universities for Research in Astronomy, Inc., for NASA, under contract NAS5-26555. The UCSC team is supported in part by NASA grants 80NSSC23K0301 and 80NSSC24K1411; and a fellowship from the David and Lucile Packard Foundation to R.J.F. C. G. is supported by a VILLUM FONDEN Young Investigator grant (VIL25501) and a Villum Experiment grant (VIL69896). M.R.S. is supported by an STScI postdoctoral fellowship.

The Young Supernova Experiment (YSE) and its research infrastructure is supported by the European Research Council under the European Union's Horizon 2020 research and innovation program (ERC grant agreement 101002652, PI K. Mandel), the Heising-Simons Foundation (2018-0913, PI R. Foley; 2018-0911, PI R. Margutti), NASA (NNG17PX03C, PI R. Foley), NSF (AST–1720756, AST–1815935, PI R. Foley; AST–1909796, AST-1944985, PI R. Margutti), the David & Lucille Packard Foundation (PI R. Foley), VILLUM FONDEN (project 16599, PI J. Hjorth), and the Center for AstroPhysical Surveys (CAPS) at the National Center for Supercomputing Applications (NCSA) and the University of Illinois Urbana-Champaign.

Pan-STARRS is a project of the Institute for Astronomy of the University of Hawai'i, and is supported by the NASA SSO Near Earth Observation Program under grants 80NSSC18K0971, NNX14AM74G, NNX12AR65G, NNX13AQ47G, NNX08 AR22G, 80NSSC21K1572, and by the State of Hawai'i. The Pan-STARRS1 Surveys (PS1) and the PS1 public science archive have been made possible through contributions by the Institute for Astronomy, the University of Hawai'i, the Pan-STARRS Project Office, the Max-Planck Society and its participating institutes, the Max Planck Institute for Astronomy, Heidelberg and the Max Planck Institute for Extraterrestrial Physics, Garching, The Johns Hopkins University, Durham University, the University of Edinburgh, the Queen's University Belfast, the Harvard-Smithsonian Center for Astrophysics, the Las Cumbres Observatory Global Telescope Network Incorporated, the National Central University of Taiwan, STScI, NASA under grant NNX08AR22G issued through the Planetary Science Division of the NASA Science Mission Directorate, NSF grant AST-1238877, the University of Maryland, Eotvos Lorand University (ELTE), the Los Alamos National Laboratory, and the Gordon and Betty Moore Foundation.

Some of the data presented herein were obtained at the W. M. Keck Observatory, which is a private 501(c)3 nonprofit organization operated as a scientific partnership among the California Institute of Technology, the University of California, and the National Aeronautics and Space Administration. The Observatory was made possible by the generous financial support of the W. M. Keck Foundation.

A major upgrade of the Kast spectrograph on the Shane 3 m telescope at Lick Observatory was made possible through generous gifts from the Heising-Simons Foundation as well as William and Marina Kast. Research at Lick Observatory is partially supported by a generous gift from Google.

The data presented here were obtained in part with ALFOSC, which is provided by the Instituto de Astrofisica de Andalucia (IAA) under a joint agreement with the University of Copenhagen and the Nordic Optical Telescope (NOT).

This work has made use of data from the Asteroid Terrestrial-impact Last Alert System (ATLAS) project. The Asteroid Terrestrial-impact Last Alert System (ATLAS) project is primarily funded to search for near Earth asteroids through NASA grants NN12AR55G, 80NSSC18K0284, and 80NSSC18K1575; byproducts of the NEO search include images and catalogs from the survey area. This work was partially funded by Kepler/K2 grant J1944/80NSSC19K0112 and HST GO-15889, and STFC grants ST/T000198/1 and ST/S006109/1. The ATLAS science products have been made possible through the contributions of the University of Hawai'i Institute for Astronomy, the Queen's University Belfast, the Space Telescope Science Institute, the South African Astronomical Observatory, and The Millennium Institute of Astrophysics (MAS), Chile.

Facilities: PS1(Pan-STARRS). The HST data used in this study can be found at MAST: doi: 10.17909/6bfs-7x11.

Software: astropy (Astropy Collaboration et al. 2013, 2018), SNooPy (C. R. Burns et al. 2011).

ORCID iDs

I. A. Abreu Paniagua https://orcid.org/0009-0007-4578-109X
W. B. Hoogendam https://orcid.org/0000-0003-3953-9532
D. O. Jones https://orcid.org/0000-0002-6230-0151
G. Dimitriadis https://orcid.org/0000-0001-9494-179X
R. J. Foley https://orcid.org/0000-0002-2445-5275
C. Gall https://orcid.org/0000-0002-8526-3963
J. O'Brien https://orcid.org/0000-0003-3615-9593
K. Taggart https://orcid.org/0000-0002-5748-4558
C. R. Angus https://orcid.org/0000-0002-4269-7999
C. Ashall https://orcid.org/0000-0002-5221-7557
K. Auchettl https://orcid.org/0000-0002-4449-9152
D. A. Coulter https://orcid.org/0000-0003-4263-2228
K. W. Davis https://orcid.org/0000-0002-5680-4660
T. de Boer https://orcid.org/0000-0001-5486-2747
A. Do https://orcid.org/0000-0003-3429-7845
H. Gao https://orcid.org/0000-0003-1015-5367
L. Izzo https://orcid.org/0000-0001-9695-8472
C.-C. Lin https://orcid.org/0000-0002-7272-5129
T. B. Lowe https://orcid.org/0000-0002-9438-3617
Z. Lai https://orcid.org/0000-0001-8483-9089
R. Kaur https://orcid.org/0009-0005-1871-7856
M. Y. Kong https://orcid.org/0009-0005-5121-2884
A. Rest https://orcid.org/0000-0002-4410-5387
M. R. Siebert https://orcid.org/0000-0003-2445-3891
S. K. Yadavalli https://orcid.org/0000-0002-0840-6940
Y. Zenati https://orcid.org/0000-0002-0632-8897
Q. Wang https://orcid.org/0000-0001-5233-6989

References

Ahumada, R., Allende Prieto, C., Almeida, A., et al. 2020, ApJS, 249, 3
Akerlof, C., Miller, J., Peters, C., et al. 2007, CBET, 2, 1059
Aleo, P. D., Malanchev, K., Sharief, S., et al. 2023, ApJS, 266, 9
Angus, C. R., & Rojas-Bravo, C. 2021, TNSCR, 1, 2021
Angus, C. R., Woosley, S. E., Foley, R. J., et al. 2024, ApJL, 977, 28

Arnett, W. D. 1982, ApJ, 253, 785
Ashall, C., Lu, J., Burns, C., et al. 2020, ApJL, 895, L3
Ashall, C., Lu, J., Hsiao, E. Y., et al. 2021, ApJ, 922, 205
Astropy Collaboration, Price-Whelan, A. M., Sipőcz, B. M., et al. 2018, AJ, 156, 123
Astropy Collaboration, Robitaille, T. P., Tollerud, E. J., et al. 2013, A&A, 558, A33
Baltay, C., Rabinowitz, D., Hadjiyska, E., et al. 2013, PASP, 125, 683
Bertin, E., & Arnouts, S. 1996, A&AS, 117, 393
Betoule, M., Kessler, R., Guy, J., et al. 2014, A&A, 568, A22
Bhattacharjee, S., Pan, Y.-C., Miao, H.-Y., et al. 2025, MNRAS, 542, 2752
Blanton, M. R., Bershady, M. A., Abolfathi, B., et al. 2017, AJ, 154, 28
Blondin, S., Matheson, T., Kirshner, R. P., et al. 2012, AJ, 143, 126
Blondin, S., & Tonry, J. L. 2007, ApJ, 666, 1024
Branch, D., Dang, L. C., Hall, N., et al. 2006, PASP, 118, 560
Brout, D., Scolnic, D., Popovic, B., et al. 2022, ApJ, 938, 110
Burke, J., Howell, D. A., Sarbadhicary, S. K., et al. 2021, ApJ, 919, 142
Burns, C. R., Parent, E., Phillips, M. M., et al. 2018, ApJ, 869, 56
Burns, C. R., Stritzinger, M., Phillips, M. M., et al. 2011, AJ, 141, 19
Burns, C. R., Stritzinger, M., Phillips, M. M., et al. 2014, ApJ, 789, 32
Caiazzo, I., Burdge, K. B., Fuller, J., et al. 2021, Natur, 595, 39
Cao, Y., Johansson, J., Nugent, P. E., et al. 2016b, ApJ, 823, 147
Cao, Y., Kulkarni, S. R., Gal-Yam, A., et al. 2016a, ApJ, 832, 86
Cao, Y., Kulkarni, S. R., Howell, D. A., et al. 2015, Natur, 521, 328
Chakradhari, N. K., Sahu, D. K., Srivastav, S., & Anupama, G. C. 2014, MNRAS, 443, 1663
Chambers, K. C., Magnier, E. A., Metcalfe, N., et al. 2016, arXiv:1612.05560
Chatzopoulos, E., Wheeler, J. C., & Vinko, J. 2012, ApJ, 746, 121
Chatzopoulos, E., Wheeler, J. C., Vinko, J., Horvath, Z. L., & Nagy, A. 2013, ApJ, 773, 76
Chen, P., Dong, S., Katz, B., et al. 2019, ApJ, 880, 35
Chevalier, R. A. 1982, ApJ, 258, 790
Chevalier, R. A., & Fransson, C. 1994, ApJ, 420, 268
Childress, M., Aldering, G., Aragon, C., et al. 2011, ApJ, 733, 3
Clemens, J. C., Crain, J. A., & Anderson, R. 2004, SPIE, 5492, 331
Coulter, D. A., Jones, D. O., McGill, P., et al. 2023, PASP, 135, 064501
Desai, D. D., Kochanek, C. S., Shappee, B. J., et al. 2024, MNRAS, 530, 5016
DES Collaboration, Abbott, T. M. C., Acevedo, M., et al. 2024, ApJL, 973, L14
Dey, A., Schlegel, D. J., Lang, D., et al. 2019, AJ, 157, 168
Dimitriadis, G., Foley, R. J., Arendse, N., et al. 2022, ApJ, 927, 78
Dimitriadis, G., Foley, R. J., Rest, A., et al. 2019, ApJL, 870, L1
Dimitriadis, G., Maguire, K., Karambelkar, V. R., et al. 2023, MNRAS, 521, 1162
Drake, A. J., Djorgovski, S. G., Mahabal, A., et al. 2009, ApJ, 696, 870
Fausnaugh, M. M., Valleley, P. J., Tucker, M. A., et al. 2023, ApJ, 956, 108
Filippenko, A. V., Richmond, M. W., Matheson, T., et al. 1992, ApJL, 384, L15
Flewelling, H. A., Magnier, E. A., Chambers, K. C., et al. 2020, ApJS, 251, 7
Folatelli, G., Morrell, N., Phillips, M. M., et al. 2013, ApJ, 773, 53
Freedman, W., Madore, B., Jang, I. S., et al. 2024, APS Meeting, 2024, S01.002
Freedman, W. L., Madore, B. F., Hatt, D., et al. 2019, ApJ, 882, 34
Ganeshalingam, M., Li, W., Filippenko, A. V., et al. 2012, ApJ, 751, 142
Garavini, G., Folatelli, G., Nobili, S., et al. 2007, A&A, 470, 411
Graham, M. L., Harris, C. E., Nugent, P. E., et al. 2019, ApJ, 871, 62
Guillochon, J., Nicholl, M., Villar, V. A., et al. 2018, ApJS, 236, 6
Hachisu, I., Kato, M., & Nomoto, K. 2008, ApJ, 679, 1390
Hicken, M., Garnavich, P. M., Prieto, J. L., et al. 2007, ApJ, 669, L17
Holmbo, S., Stritzinger, M. D., Karamehmetoglu, E., et al. 2023, A&A, 675, A83
Holoien, T. W. S., Stanek, K. Z., Kochanek, C. S., et al. 2015, ATel, 7450, 1
Hoogendam, W. B., Ashall, C., Galbany, L., et al. 2022, ApJ, 928, 103
Hoogendam, W. B., Ashall, C., Jones, D. O., et al. 2025b, ApJ, 988, 209
Hoogendam, W. B., Jones, D. O., Ashall, C., et al. 2025a, OJAp, 8, 22
Hoogendam, W. B., Shappee, B. J., Brown, P. J., et al. 2024, ApJ, 966, 139
Hook, I. M., Jørgensen, I., Allington-Smith, J. R., et al. 2004, PASP, 116, 425
Howell, D. A., Sullivan, M., Nugent, P. E., et al. 2006, Natur, 443, 308
Howell, D. A., Sullivan, M., Perrett, K., et al. 2005, ApJ, 634, 1190
Hoyle, F., & Fowler, W. A. 1960, ApJ, 132, 565
Hsiao, E. Y., Conley, A., Howell, D. A., et al. 2007, ApJ, 663, 1187
Hsiao, E. Y., Hoeflich, P., Ashall, C., et al. 2020, ApJ, 900, 140
Iben, I. J., & Tutukov, A. V. 1984, ApJS, 54, 335
Ilkov, M., & Soker, N. 2013, MNRAS, 428, 579
Jiang, J.-a., Doi, M., Maeda, K., et al. 2017, Natur, 550, 80
Jiang, J.-a., Maeda, K., Kawabata, M., et al. 2021, ApJL, 923, L8
Johnson, B. D., Leja, J., Conroy, C., & Speagle, J. S. 2021, ApJS, 254, 22
Jones, D. O., Foley, R. J., Narayan, G., et al. 2021, ApJ, 908, 143
Jones, D. O., McGill, P., Manning, T. A., et al. 2024, arXiv:2410.17322
Jones, D. O., Scolnic, D. M., Foley, R. J., et al. 2019, ApJ, 881, 19
Kaiser, N. & Pan-STARRS Team 2002, AAS Meeting, 201, 122.07
Kasen, D. 2010, ApJ, 708, 1025
Kashi, A., & Soker, N. 2011, MNRAS, 417, 1466
Khatami, D. K., & Kasen, D. N. 2019, ApJ, 878, 56
Krisciunas, K., Contreras, C., Burns, C. R., et al. 2017, AJ, 154, 211
Kromer, M., Fremling, C., Pakmor, R., et al. 2016, MNRAS, 459, 4428
Kurtz, M. J., Mink, D. J., Wyatt, W. F., et al. 1992, ASPC, 25, 432
Kutsuna, M., & Shigeyama, T. 2015, PASJ, 67, 54
Kwok, L. A., Jha, S. W., Temim, T., et al. 2023, ApJL, 944, L3
Kwok, L. A., Siebert, M. R., Johansson, J., et al. 2024, ApJ, 966, 135
Leibundgut, B., Kirshner, R. P., Phillips, M. M., et al. 1993, AJ, 105, 301
Leja, J., Johnson, B. D., Conroy, C., van Dokkum, P. G., & Byler, N. 2017, ApJ, 837, 170
Leung, S.-C., Diehl, R., Nomoto, K., & Siegert, T. 2021, ApJ, 909, 152
Leung, S.-C., & Nomoto, K. 2020, ApJ, 888, 80
Levanon, N., & Soker, N. 2017, MNRAS, 470, 2510
Levanon, N., Soker, N., & García-Berro, E. 2015, MNRAS, 447, 2803
Li, W., Filippenko, A. V., Chornock, R., et al. 2003, PASP, 115, 453
Livne, E. 1990, ApJL, 354, L53
Lu, J., Ashall, C., Hsiao, E. Y., et al. 2021, ApJ, 920, 107
Maeda, K., an Jiang, J., Shigeyama, T., & Doi, M. 2018, ApJ, 861, 78
Maeda, K., Jiang, J.-a., Doi, M., Kawabata, M., & Shigeyama, T. 2023, MNRAS, 521, 1897
Maeda, K., Kutsuna, M., & Shigeyama, T. 2014, ApJ, 794, 37
Magee, M. R., & Maguire, K. 2020, A&A, 642, A189
Magee, M. R., Maguire, K., Kotak, R., et al. 2020, A&A, 634, A37
Magnier, E. A., Chambers, K. C., Flewelling, H. A., et al. 2020a, ApJS, 251, 3
Magnier, E. A., Sweeney, W. E., Chambers, K. C., et al. 2020b, ApJS, 251, 5
Martin, D. C., Fanson, J., Schiminovich, D., et al. 2005, ApJL, 619, L1
Miller, A. A., Magee, M. R., Polin, A., et al. 2020b, ApJ, 898, 56
Miller, A. A., Yao, Y., Bulla, M., et al. 2020a, ApJ, 902, 47
Miller, J. S., & Stone, R. P. S. 1994, The KAST Double Spectrograph 66, Lick Observatory Techinical Report
Moriya, T. J., Liu, D., Wang, B., & Liu, Z.-W. 2019, MNRAS, 488, 3949
Morokuma, T., Mazzali, P., Piascik, A., et al. 2015, ATel, 7532, 1
Morrell, N., Phillips, M. M., Folatelli, G., et al. 2024, ApJ, 967, 20
Nadyozhin, D. K. 1994, ApJS, 92, 527
Nicholl, M. 2018, RNAAS, 2, 230
Nomoto, K. 1980, in Type I Supernovae in Texas Workshop, ed. J. C. Wheeler, 164
Nomoto, K. 1982a, ApJ, 253, 798
Nomoto, K. 1982b, ApJ, 257, 780
Nomoto, K., Thielemann, F. K., & Yokoi, K. 1984, ApJ, 286, 644
O'Hora, J., Ashall, C., Shahbandeh, M., et al. 2025, ApJ, 984, 34
Oke, J. B., Cohen, J. G., Carr, M., et al. 1995, PASP, 107, 375
Pakmor, R., Kromer, M., Röpke, F. K., et al. 2010, Natur, 463, 61
Parrent, J. T., Howell, D. A., Fesen, R. A., et al. 2016, MNRAS, 457, 3702
Perets, H. B., Zenati, Y., Toonen, S., & Bobrick, A. 2019, arXiv:1910.07532
Phillips, M. M. 1993, ApJL, 413, L105
Phillips, M. M., Ashall, C., Brown, P. J., et al. 2024, ApJS, 273, 16
Phillips, M. M., Lira, P., Suntzeff, N. B., et al. 1999, AJ, 118, 1766
Phillips, M. M., Wells, L. A., Suntzeff, N. B., et al. 1992, AJ, 103, 1632
Pier, E. A., & Chambers, K. 2007, AAS Meeting, 210, 82.08
Piro, A. L., & Morozova, V. S. 2016, ApJ, 826, 96
Polin, A., Nugent, P., & Kasen, D. 2019, ApJ, 873, 84
Puckett, T., Moore, R., Newton, J., & Orff, T. 2009, CBET, 1762, 1
Raskin, C., Timmes, F. X., Scannapieco, E., Diehl, S., & Fryer, C. 2009, MNRAS, 399, L156
Riess, A. G., Yuan, W., Macri, L. M., et al. 2022, ApJL, 934, L7
Rosswog, S., Kasen, D., Guillochon, J., & Ramirez-Ruiz, E. 2009, ApJL, 705, L128
Ruiter, A. J., & Seitenzahl, I. R. 2025, A&ARv, 33, 1
Sarin, N., Hübner, M., Omand, C. M. B., et al. 2024, MNRAS, 531, 1203
Scalzo, R. A., Aldering, G., Antilogus, P., et al. 2010, ApJ, 713, 1073
Scolnic, D. M., Jones, D. O., Rest, A., et al. 2018, ApJ, 859, 101
Shappee, B. J., Holoien, T. W.-S., Drout, M. R., et al. 2018, ApJ, 870, 13
Shen, K. J., Bildsten, L., Kasen, D., & Quataert, E. 2012, ApJ, 748, 35
Shen, K. J., & Moore, K. 2014, ApJ, 797, 46
Shingles, L., Smith, K. W., Young, D. R., et al. 2021, TNSAN, 7, 1
Siebert, M. R., Foley, R. J., Jones, D. O., et al. 2019, MNRAS, 486, 5785
Siebert, M. R., Kwok, L. A., Johansson, J., et al. 2024, ApJ, 960, 88
Silverman, J. M., Ganeshalingam, M., Li, W., et al. 2011, MNRAS, 410, 585

Skrutskie, M. F., Cutri, R. M., Stiening, R., et al. 2006, AJ, 131, 1163
Smith, K. W., Smartt, S. J., Young, D. R., et al. 2020, PASP, 132, 085002
Soker, N., & Bear, E. 2023, MNRAS, 521, 4561
Srivastav, S., Moore, T., Nicholl, M., et al. 2023, ApJL, 956, L34
Srivastav, S., Smartt, S. J., Huber, M. E., et al. 2023, ApJL, 943, L20
Stritzinger, M., Mazzali, P. A., Sollerman, J., & Benetti, S. 2006, A&A, 460, 793
Taubenberger, S. 2017, The Extremes of Thermonuclear Supernovae (Springer International Publishing), 317
Taubenberger, S., Benetti, S., Childress, M., et al. 2011, MNRAS, 412, 2735
Thornton, I., Villar, V. A., Gomez, S., & Hosseinzadeh, G. 2024, RNAAS, 8, 48
Tody, D. 1986, SPIE, 627, 733
Tonry, J., Denneau, L., Heinze, A., et al. 2021, TNSTR, 2021-2159, 1
Tonry, J. L., Denneau, L., Heinze, A. N., et al. 2018, PASP, 130, 064505
Tsebrenko, D., & Soker, N. 2015, MNRAS, 447, 2568
Tucker, M. A., Ashall, C., Shappee, B. J., et al. 2021, ApJ, 914, 50
Wang, B., Leja, J., Villar, V. A., & Speagle, J. S. 2023, ApJL, 952, L10
Wang, Q., Rest, A., Dimitriadis, G., et al. 2024, ApJ, 962, 17
Webbink, R. F. 1984, ApJ, 277, 355
Whelan, J., & Iben, I., Jr. 1973, ApJ, 186, 1007
Wright, E. L., Eisenhardt, P. R. M., Mainzer, A. K., et al. 2010, AJ, 140, 1868
Xi, G., Wang, X., Li, G., et al. 2024, MNRAS, 527, 9957
Ye, C., Jones, D. O., Hoogendam, W. B., et al. 2024, ApJ, 974, 164
York, D. G., Adelman, J., Anderson, J. E., Jr., et al. 2000, AJ, 120, 1579